# Investigation of an Inverted Meniscus Heat Pipe Wick Concept

## NASA CR-137,724

## August 1975



by E. W. Saaski
Manager, Thermal Systems
Sigma Research, Inc.
2952 George Washington Way
Richland, Washington 99352



Prepared for
Ames Research Center
National Aeronautics and Space Administration
Moffet Field, California 94035

# INVESTIGATION OF AN INVERTED MENISCUS HEAT PIPE WICK CONCEPT

NASA CR-137,724

August 1975

by E. W. Saaski

Manager, Thermal Systems
Sigma Research, Inc.
2952 George Washington Way
Richland, Washington 99352

Prepared for
Ames Research Center
National Aeronautics and Space Administration
Moffett Field, California 94035

*ABSTRACT*

*This report describes a new wicking concept for efficient evaporation of heat pipe working fluids under diverse conditions. It embodies the high heat transfer coefficient of the circumferential groove while retaining the circumferential fluid transport capability of a thick porous wick or screen. Experimental tests are described which substantiate the efficacy of the evaporation technique for a circumferentially-grooved heat pipe charged alternately with ammonia and R-11 ($CCl_3F$). With ammonia, heat transfer coefficients in the range of 2 to 2.7 $W/cm^2{}^\circ K$ were measured at heat flux densities up to 20 $W/cm^2$ while, with R-11, a heat transfer coefficient of 1.0 $W/cm^2{}^\circ K$ was measured with flux densities up to 5 $W/cm^2$. Heat transfer coefficients and flux densities were unusually high compared to literature data for other nonboiling evaporative surfaces, and it is suggested that this enhancement may be either due to film turbulence generated by vapor shear or convective cells driven by surface-tension gradient.*

# CONTENTS

## LIST OF FIGURES

## LIST OF FIGURES (CONTINUED)

## SYMBOL TABLE

| | |
|---|---|
| $A$ | Single groove cross-sectional area, $cm^2$ |
| $C_p$ | Fluid specific heat, Joules/g °K |
| $D$ | Heat pipe diameter at grooves, cm |
| $FOM_i$ | Inverted meniscus vapor flow figure of merit |
| $\overline{H}$ | Overall evaporative heat transfer coefficient, $W/cm^2$ °K |
| $H_{fg}$ | Latent heat of vaporization, Joules/g-mole |
| $h_m$ | Maximum fluid rise height, cm |
| $K_f$ | Fluid thermal conductivity, W/cm °K |
| $K_p$ | Wick permeability, $cm^2$ |
| $L$ | Evaporator axial length, cm |
| $M$ | Number of axial slits in transport wicking, transverse grooves |
| $M_a$ | Fluid molecular weight, g/g-mole |
| $N$ | Linear density of transverse grooves, $cm^{-1}$ |
| $P$ | Wetted internal perimeter of groove, excluding any covering, cm |
| $\Delta P_\ell$ | Total condensate liquid pressure drop from condenser end to an evaporator position, $dynes/cm^2$ |
| $\Delta P_v$ | Vapor pressure difference in vapor microchannel due to laminar viscous vapor flow, $dynes/cm^2$ |
| $\Delta P_{em}$ | Maximum liquid pressure drop in evaporator, when $Q = Q_m$, $dynes/cm^2$ |
| $\Delta P_{vm}$ | Maximum groove vapor pressure drop when $Q = Q_m$, $dynes/cm^2$ |
| $Q_a$ | Area-averaged evaporative heat flux density, $W/cm^2$ |
| $Q$ | Overall evaporator heat flux, watts |
| $Q_m$ | Maximum overall evaporator heat flux, where total fluid pressure drop = $2\gamma/r_c$, watts |
| $R$ | Vapor microchannel effective radius for vapor flow modeling, cm |
| $R_a$ | Artery radius, cm |

## SYMBOL TABLE (CONTINUED)

| | |
|---|---|
| $r_c$ | Effective capillary pore radius for fluid transport wicking, cm |
| $\Delta T_{ev}$ | Temperature difference across evaporative film, °K |
| W | Groove width, cm |
| Z | Axial position in evaporator, with Z = 0 at end nearest condenser, cm |
| $Z_m$ | Axial position corresponding to fluid pressure drop $\Delta P_\ell$ |
| $\epsilon$ | Ratio of microchannel pressure drop to condensate pressure drop |
| $\epsilon'$ | Ratio of microchannel pressure drop to maximum capillary priming potential |
| $\gamma$ | Fluid surface tension, dynes/cm |
| $\gamma'$ | rate of change of surface tension with temperature, dynes/cm °K |
| $\eta$ | Ratio of maximum microchannel pressure drop to maximum fluid pressure drop in evaporator |
| $\pi_e$ | Maximum dimensionless liquid pressure drop in evaporator, corresponding to $Q = Q_m$, and defined as $\pi_e = \Delta P_{em}/(2\gamma/r_c)$ |
| $\pi_v$ | Maximum dimensionless groove pressure drop, corresponding to $Q = Q_m$, defined as $\pi_v = \Delta P_{vm}/(2\gamma/r_c)$ |
| $\rho_v$ | Vapor density, $g/cm^3$ |
| $\rho_f$ | fluid density, $g/cm^3$ |
| $\psi$ | Groove angle, degrees |
| $\mu_v$ | Vapor viscosity, poise |
| $\mu_f$ | Fluid viscosity, poise |
| $\chi$ | $\cos(\psi/2)/[1 + \sin(\psi/2)]$ |
| $\delta$ | Film thickness, cm |

# INVESTIGATION OF AN INVERTED MENISCUS HEAT PIPE WICK CONCEPT

## 1. INTRODUCTION

Over the last ten years, the heat pipe has been developed into a valuable thermal control device for varied aerospace and terrestrial applications. Significant advances have been made in increasing the maximum heat transport capacity of heat pipes by various types of wicking strategies. In some cases, however, these transport improvements have sacrificed operational stability because of sensitivity to shock or noncondensable gases, for example.

Similarly, improvements toward reducing temperature differences associated with heat injection and rejection have not been without disadvantage. For example, the use of a thinner layer of wicking on the heat pipe inner wall to reduce the fluid film temperature drop may create manufacturing problems due to the flexibility of such wicks. This lack of stiffness can result in poor contact of the wick with the wall and may lead to vapor void formation and associated hot spots. In addition, the more fine-pored wicks have very low fluid permeabilities, and circumferential fluid transport may not be adequate. Another approach to minimize gradients, the use of fine circumferential V-grooves in conjunction with a high permeability axial wicking, has received a great deal of attention recently. This technique offers a very low heat transfer resistance, but the required thread density (40 or more grooves/cm) is difficult to attain, and for fluids of high density and/or low surface tension, the circumferential fluid transport rates may not be adequate within the small grooves.

This report describes in Section 2, Technical Discussion, a new wicking concept, the inverted meniscus, for efficient evaporation of heat pipe working fluids under diverse conditions. It embodies the high heat transfer coefficient of the circumferential groove, while retaining the circumferential fluid transport capability of a thick porous wick or screen.

Verification of this wicking concept is presented in Section 3, Experimental Testing. Both open grooved and inverted meniscus evaporators were tested to establish relative heat transfer effectiveness.

Section 4, Summary, discusses potential applications for this type of evaporative surface and identifies several areas which merit further investigation along the lines of improving surface efficiency and developing physical models for the unusually high heat transfer coefficients measured.

## 2. TECHNICAL DISCUSSION

### 2.1 Present Wick Concepts

It is useful to initially define the function of circumferential wicking within a heat pipe, and to identify basic types employed historically or presently. Physically, heat transferred into a heat pipe produces a conduction drop through the heat pipe wall, and another drop through any fluid films present on the inner side of the wall. Since the heat pipe relies on this fluid for the evaporation process, the film is a necessary component. However, it is well documented that the primary internal temperature drop associated with heat transfer in most heat pipes is the fluid conduction drop, so that it is imperative to minimize the fluid film thickness and employ fluids of high thermal conductivity. Fluids as a class are unfortunately poor conductors, with thermal conductivities on the order of 0.001 to 0.005 W/cm $^{\circ}$K.

Two techniques for fluid distribution which have been used for some time are the felt-metal wick and the wire cloth wick. Each is essentially a fine-pored metal capillary material which is tightly held against the wall. For low power operation, these wicks are adequate to transport condensate axially back to the evaporator, as well as circumferentially within the evaporator. However, for common low temperature fluids, power levels above several watts require additional wicking to transport liquid from the condenser to the evaporator by capillary action. Most heat pipes now employ a by-pass wicking which has a high permeability for axial flow, so that the fluid flow pattern is essentially axial within this high fluid conductance wick, and circumferential within the wall wicking, the circumferential wicking being fed by the axial wicking along one or more contact lines between the two types of wick.

The felt metal and screen wicks have three potential disadvantages. Because of low thermal conductivity, even thin fluid films on the order of 0.01 to 0.02 cm thickness can create undesirably high film temperature drops. Besides being undesirable from a thermal standpoint, the resulting wall superheat promotes nucleate boiling at nucleation sites on the heat pipe wall, severely impeding heat transfer and fluid flow within the film.

It is also difficult to find wicking materials with the proper combination of flexibility or stiffness to seat tightly against the heat pipe wall, especially if the wicking is a fine-pore screen of 400 mesh per inch, for example. Large gaps can be produced locally between wick and wall which produce nonuniform evaporator characteristics or, under worst conditions, boiling is initiated and a large vapor block forms. In addition, circumferential flow of

liquid from the by-pass wick through the wall wicking may be impeded by the high flow resistance of the thin, fine-woven screen, causing wick dry-out in the zones farthest away from the by-pass wicking contact lines.

The primary alternative method of fluid distribution is the capillary groove. The wall wicking consists of either axial or circumferential grooves extruded or cut into the heat pipe wall. Typical grooves in an axially-grooved heat pipe are large, on the order of 0.1 cm square. The grooves are optimum at a rather large size since the grooves are used for condensate transport from the condenser, in addition to evaporation.

The circumferentially grooved pipe is generally produced by a threading or machining operation with from 20 to 200 threads per inch. Condensate is fed to the threads using some type of by-pass wicking. The permeability-area product ($K_pA$) for a single groove may be low, and for fluids of high density and/or low surface tension, the circumferential pressure drop may be high. That is, moderate heat fluxes may dry out the grooves and render them ineffectual. Open grooves are always inferior in surface tension pumping to square-weave screen of the same characteristic dimension since an open groove has only one principal radius of curvature whereas screen of comparable pore size has two principal radii of curvature. Response of open grooves to adverse tilt is greater, and maximum capacity is lower than screen when capillary pumping is the limiting factor in heat transport.

Evaporation in grooves of all sizes can be shown to preferentially occur at the areas of minimum film thickness, as in Figure 2.1. Therefore, although the liquid film is discontinuous, the extremely high local heat transfer coefficients associated with fillet evaporation yield a reasonably high heat transfer coefficient with open grooves.

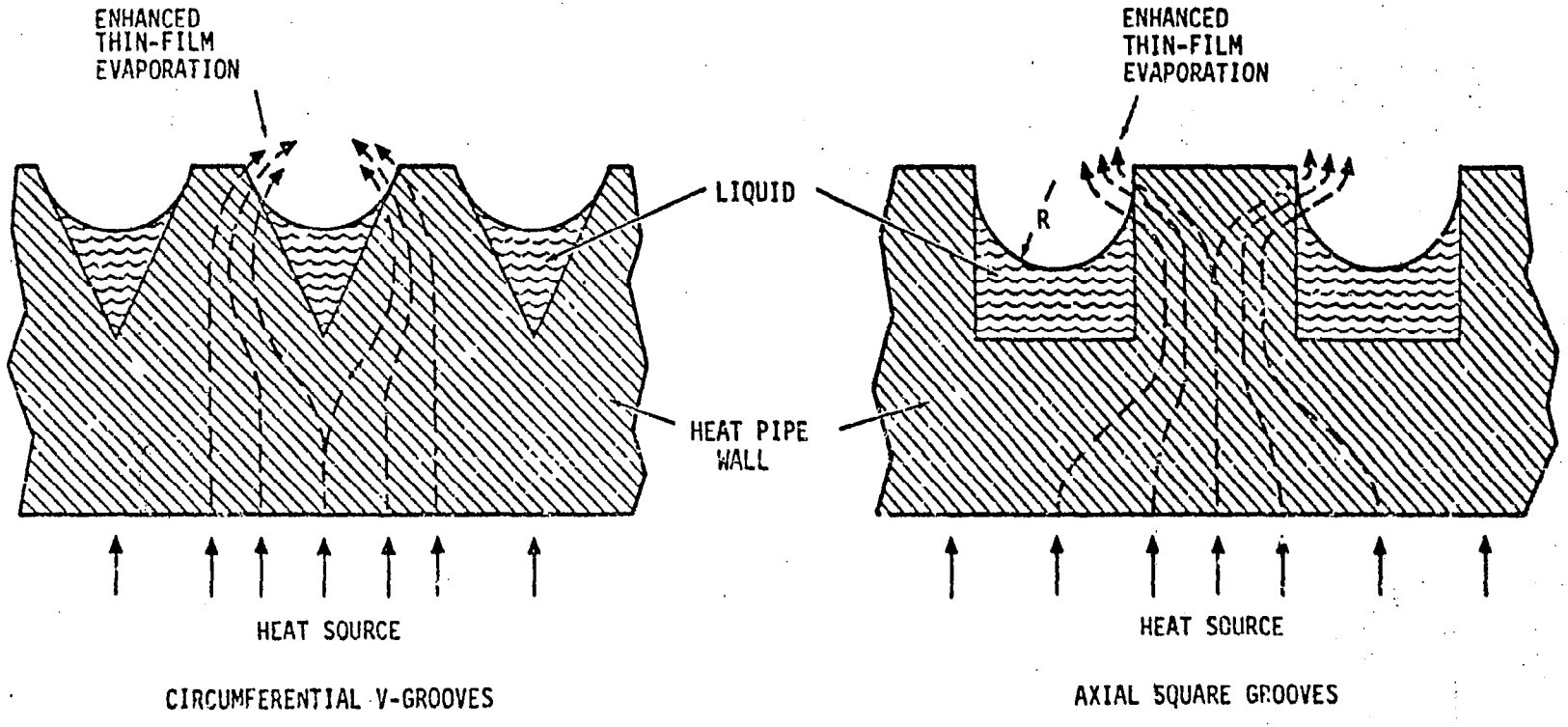


FIGURE 2.1. EVAPORATIVE HEAT TRANSFER FROM AN OPEN GROOVE

## 2.2 High Performance Inverted Meniscus Wick

In the previous section, pros and cons of various wicking concepts have been discussed. To summarize, screens and felt-metals provide good capillary pumping capability, but can have a low heat transfer coefficient, while grooves obtain high heat transfer coefficients but suffer a lower pumping capability either in terms of maximum power or maximum adverse tilt in 1-g. However, the permeability of screen wicking is typically less than that for grooves. The wicking concept proposed retains favorable elements of both fundamental liquid distribution means.

The new wicking concept is shown applied to an axially-grooved heat pipe in Figure 2.2. Accompanying detail sketches of Figure 2.2 show differences between the new evaporative wicking and screen and open groove wicking. In operation, the wicking distributes fluid circumferentially through a thick felt-metal member, or multilayer screen member in intimate contact with the axial grooves. At modest power levels, the covered grooves will deprime partially as shown in Detail A due to excessive superheat and/or capillary pressure constraints. The inverted menisci then formed provide an extremely efficient means of evaporative heat transfer, similar to the conventional menisci in Figure 2.1. Vapor evolved from the double meniscus flows in each microchannel to an open end of the groove, where the vapor is then transported axially to the condenser via the central heat pipe vapor core.

In a spirally-grooved evaporator, evaporation and vapor flow also occur as described above. In the latter case, however, it is necessary to provide axial slits for communication of vapor from the circumferential grooves to the heat pipe core. One method for achieving this, as used for the laboratory proof-of-principle tests, is described in Section 3.

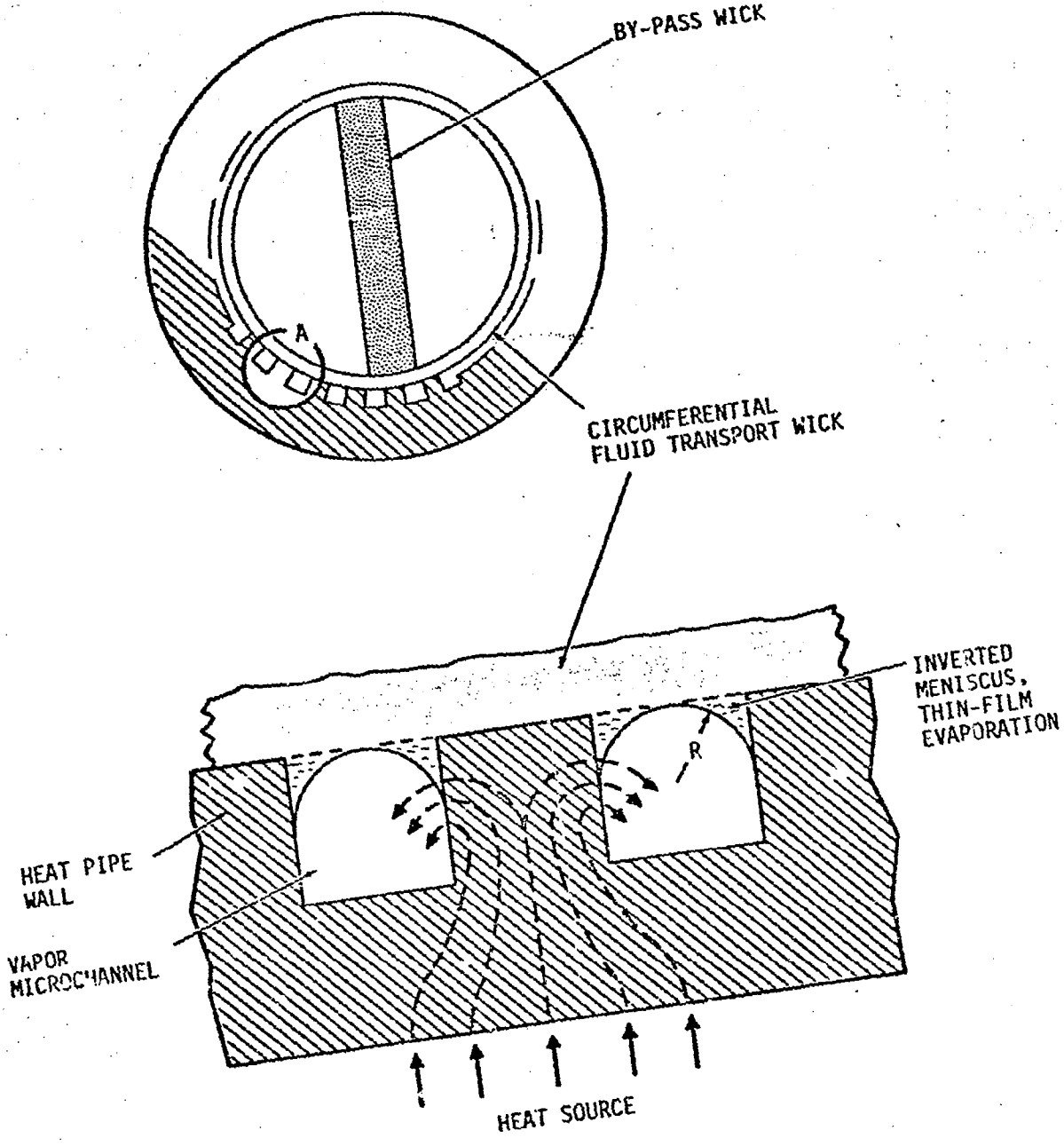


FIGURE 2.2. HIGH PERFORMANCE HYBRID WICK

Since heat transfer occurs predominantly through the menisci, the thick, high permeability transport wicking covering the grooves can be optimized for fluid flow and capillary pore size, since it is not an integral part of the evaporative wicking, as in circumferential screen wicking. It may be possible to extend the maximum heat transfer limits for arteryless heat pipes by increasing the thickness of this transport wick, and eliminate many problems related to arterial failure. In addition, the separation of fluid transport and heat transfer mechanisms allows operation at much higher radial heat fluxes, by increasing circumferential wicking capacity without increasing the evaporative film thickness, and the potential for nucleate boiling.

In the conventional groove of Figure 2.1, the radius of curvature can decrease only a modest amount before the fillets have such a small cross-section that the evaporator dries out. For the inverted meniscus evaporative wick, the final radius achievable is limited by pore size of the transport wick covering the grooves since the fillets themselves contribute only a minor amount to axial and circumferential fluid transport.

If a material of small pore size is used for the transport wick, fluids possessing poor surface tension and/or high density can be utilized with a much coarser groove than might otherwise be practical with satisfactory heat transfer coefficients. This may be particularly attractive for the cryogenic working fluids which, as a class, are typically of low priming capability and low thermal conductivity.

The following sections describe analyses which establish performance limits for the inverted meniscus wick.

## 2.3 Vapor Flow Constraints - Circumferential Grooves

The primary theoretical requirement for inverted meniscus operation is maintenance of an adequately low vapor pressure drop in each channel. That is, if the pressure-temperature rise is too great at a point distant from the vapor emission slot, then the meniscus will recede into the fluid distribution wick in that area and greatly inhibit local heat transfer. For this not to occur, the pressure rise due to laminar viscous flow of vapor must be some $\epsilon$ of the maximum capillary pressure difference $2\gamma/r_c - \Delta P_\ell\ (z,\theta)$, for grooves at distance $z,\theta$ from the condenser and at angular position $\theta$ on the circumference. The factor $\epsilon$ must be strictly less than 1.

$$\frac{\Delta P_v}{2\gamma/r_c - \Delta P_\ell\ (z,\theta)} = \epsilon \qquad (\epsilon \leq 1) \qquad (1)$$

We will assume that the vapor pressure drop in the primary heat pipe vapor core is negligible. For convenience the liquid pressure drop in the wicking attributable to fluid transport, $\Delta P_{\ell\theta}$, will be treated as a part of $\epsilon'$, so that

$$\frac{\Delta P_v}{2\gamma/r_c} = \epsilon' \qquad (\epsilon' \leq 1) \qquad (2)$$

For purposes of calculating the maximum viscous vapor pressure rise relative to the vapor core, it is assumed that the vapor channel is a cylinder represented in cross section by the inscribed circle (see Figure 2.3). For a V-groove, the inscribed circle has radius

$$R = 1/2\ W \cos(\psi/2)/[1 + \sin(\psi/2)] = \frac{W}{2} \cdot \chi(\psi) \qquad (3)$$

where W is groove width and $\psi$ is the groove angle. By assuming uniform heat addition per unit length of groove, a groove density of N per cm and laminar

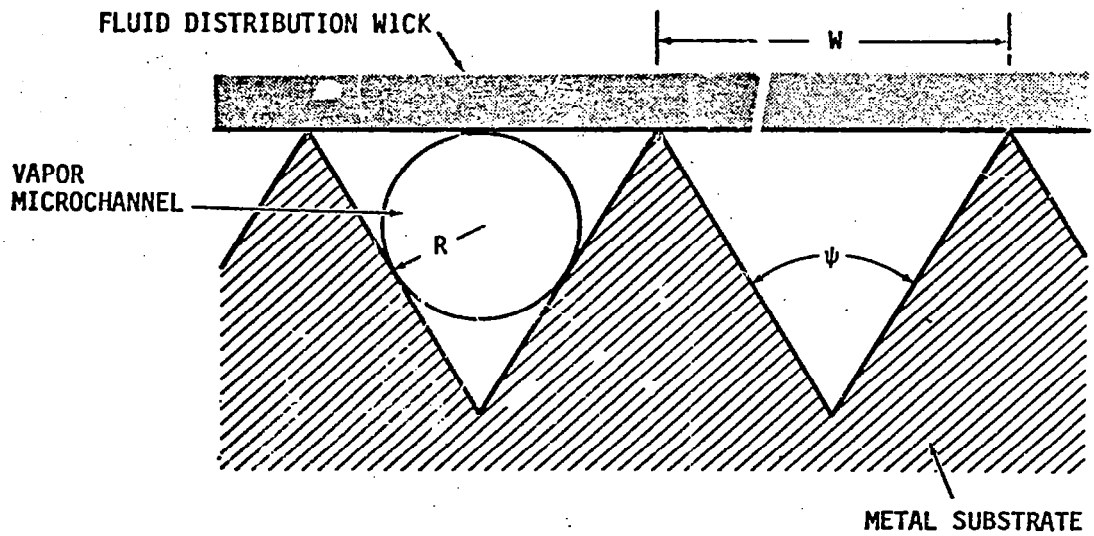


FIGURE 2.3. IDEALIZED V-GROOVE MODEL FOR ESTIMATING EFFECT OF VAPOR PRESSURE RISE ON WICK PERFORMANCE

viscous vapor flow, then the maximum area-averaged heat flux for a cylindrical evaporator is

$$Q_a = \frac{\varepsilon' M^2 \chi^4}{8\pi} \left(\frac{\rho_v \gamma H_{fg}}{\mu_a u_v}\right) \frac{1}{N^3 D^2 r_c} \qquad (W/cm^2) \qquad (4)$$

where M is the number of axial vent slots around the circumference, and D is based on the heat pipe grooved inner diameter.

The quantity in parantheses is a vapor property figure of merit. By tabulating this factor for several temperatures and by choosing representative heat pipe physical dimensions, $Q_a$ has been calculated for the fluids ammonia, methanol and methane. Fixed physical inputs are as follows:

$\varepsilon' = 0.25$

$M = 1.0$

$\psi = 60^o$

$D = 1$ cm

$r_c = 0.0032$ cm (400 mesh square-weave screen)

An $\varepsilon'$ of 0.25 was chosen as an estimate of the maximum fraction of capillary pressure expendable on vapor pressure rise. If in fact $\varepsilon'$ were 0.0625, then calculated values of $Q_a$ would still be valid if two vapor release slots were used (M = 2). That is to say, the estimates are regarded as being reasonable from the standpoint of engineering feasibility. It is also true for fluids such as ammonia that the maximum heat fluxes are so high that quite low values of $\varepsilon'$ do nct severely limit practical application of this evaporative wicking.

Table 1 presents values of the vapor figure of merit for the three fluids. Ammonia is clearly a superior fluid on this basis. Calculated values of the maximum heat flux density versus groove density are presented in Figure 2.4. An additional constraint line has been selected representing a limit of groove density based on current manufacturing techniques. This has been assumed to be approximately 80 grooves per cm, or 200 grooves per inch. For a given temperature, the figure shows that operation at higher flux densities requires fewer V-grooves be used. This is because V-grooves as in Figure 2.3 must be increased in cross-sectional area to accommodate a higher vapor flux.

Table 2 shows the maximum heat flux densities that can be obtained per equation (4) and Figure 2.4 for the reference design using the three fluids and 40 and 80 grooves/cm. With the exception of methanol, the indicated flux densities are extremely high, and exceed 100 $W/cm^2$ for ammonia. Flux densities of this magnitude may be of academic interest only, since the corresponding temperature drops are extremely large. Kosson et al have observed a maximum heat transfer coefficient of about 2.0 $W/cm^2\ ^\circ K$ for $N = 63\ cm^{-1}$ and ammonia (reference 1). As discussed in Section 3, comparable or larger heat transfer coefficients have also been obtained with an inverted meniscus heat pipe, but a heat flux of 100 $W/cm^2$ would still represent a film drop of about 50°C. This is not only thermally unacceptable but other physical phenomena would come into play to render the analysis invalid. These would include sonic limitations, entrainment limitations, vapor flow turbulence effects, boiling effects, and excessive axial pressure drops.

TABLE 1. VAPOR PROPERTY FIGURE OF MERIT FOR THE PRESSURE CONSTRAINT ASSOCIATED WITH INVERTED MENISCUS DESIGN

| Fluid | Temperature | Figure of Merit ($FOM_1$) |
|---|---|---|
| Methanol | 0 °C | 10,820 W/cm$^2$ |
| | 30 | 49,900 |
| | 60 | 153,000 |
| Methane | -180 °C | 84,000 |
| | -160 | 312,000 |
| | -140 | 607,000 |
| Ammonia | -30 °C | 503,000 |
| | 0 | 1.07 ($10^6$) |
| | 20 | 1.46 ($10^6$) |
| | 40 | 1.78 ($10^6$) |

TABLE 2. MAXIMUM HEAT FLUX DENSITIES FOR REFERENCE DESIGN INVERTED MENISCUS HEAT PIPE AND THREE TYPICAL FLUIDS

| | | Flux Density | |
|---|---|---|---|
| Fluid | Temperature | 40 cm$^{-1}$ | 80 cm$^{-1}$ |
| Methanol | 0 °C | 3.8 W/cm$^2$ | 0.48 W/cm$^2$ |
| | 30 | 18.0 | 2.25 |
| Methane | -180 | 23.0 | 2.8 |
| | -160 | 86.0 | 11.0 |
| Ammonia | -30 | >100.0 | 23.0 |
| | 0 | >100.0 | 50.0 |
| | 40 | >100.0 | 79.0 |

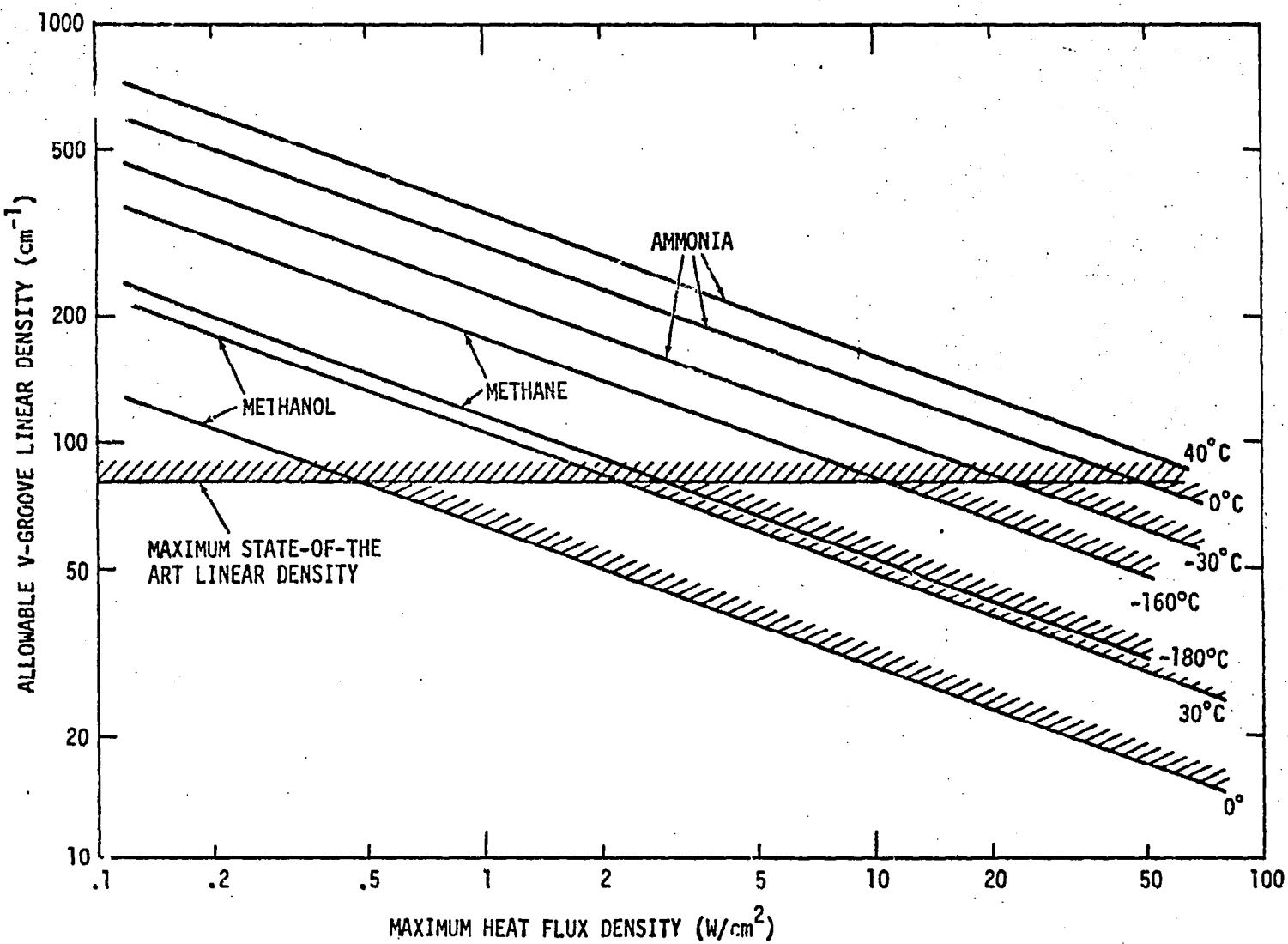


FIGURE 2.4. RELATIONSHIP BETWEEN GROOVE DENSITY AND MAXIMUM HEAT FLUX DENSITY FOR DESIGN CONDITIONS SPECIFIED IN TEXT

## 2.4 Vapor Flow Constraints - Axial Inverted Meniscus Design

### 2.4.1 Adiabatic-Evaporator Termination Methods

Experiments discussed in Section 3 show that inverted meniscus operation is often initiated by groove boiling. For an axially grooved heat pipe, this could lead to interruption of fluid flow in the grooves at the evaporator-adiabatic interface even if the covering wick is left open at both ends. Vapor evolution from the condenser end can disrupt axial fluid communication between the circumferential wick and the adiabatic grooves.

To prevent this, two different approaches are suggested. Each requires an axial by-pass wick at the adiabatic-evaporator juncture. If a serrated washer were made that closely fitted the groove conformation and blocked the groove cross section, then the circumferential wick could be butted up against this washer to form a vapor-tight seal at the adiabatic-evaporator interface. A by-pass wick would then pass through the hollow center of the washer to communicate with the adiabatic fluid through another circumferential transport wick.

In the second design concept, vapor is allowed to issue from both ends of the evaporator axial grooves. A by-pass wick would again be used, and would couple with another groove-communicating wick in the adiabatic section. For axial grooves, the inverted meniscus may be difficult to test as intercommunication in the adiabatic could deprime upper grooves in 1-g. However, if axial grooves are used in the evapurator only and a by-pass wick is used in the remainder of the heat pipe, then groove deprime is not a prcblem.

### 2.4.2 Vapor Flow Pressure Differentials

For axial grooves, calculations below establish the axial position where the vapor-liquid pressure difference is a maximum. This point is then

the most critical in terms of fluid recession into the fluid transport wick and initiation of dry-out. Details of fluid pressure-drop derivations are given in Appendix A.

Assuming uniform heat loss along the evaporator length, the liquid pressure drop for an axial wick of constant cross section and permeability is

$$\Delta P_\ell = \frac{2\gamma}{r_c}\frac{Q}{Q_m}\left\{1 - \pi_e\left[1 - \frac{2Z}{L} + \left(\frac{Z}{L}\right)^2\right]\right\} \tag{5}$$

where $\Delta P_\ell$ is relative to a constant-pressure central vapor core, and Z is the axial position relative to the evaporator end nearest the condenser. Other terms are given in the symbol table.

The vapor pressure rise in a single groove is expressible as

$$\Delta P_v = \frac{8\gamma}{r_c}\frac{Q}{Q_m}\left[\frac{Z}{L} - \left(\frac{Z}{L}\right)^2\right]\pi_v \tag{6}$$

or

$$\Delta P_v = \frac{2\gamma}{r_c}\frac{Q}{Q_m}\left[1 - \left(\frac{Z}{L}\right)^2\right]\pi_v \tag{7}$$

depending on whether the groove is open or closed at the condenser end, respectively.

From equation (3), we see that the liquid pressure drop increases with increasing Z, while the groove vapor pressure is a maximum at either $Z = \frac{L}{2}$ or $Z = 0$, depending on whether the groove is open or closed at the condenser end.

Therefore, the maximum pressure difference between the constrained vapor and the covering liquid film occurs generally between the two extremes. The total vapor-liquid pressure differential in a groove is obtained by adding $\Delta P_\ell$ and $\Delta P_v$, since they are referenced to the constant-pressure vapor core and diverge from this reference pressure. When this sum is differentiated and set equal to zero, the maximum pressure differentials are found at

$$\left(\frac{Z}{L}\right)_{crit} = \frac{1 + 2\eta}{1 + 4\eta} \qquad \text{(open ends)} \qquad (8)$$

or $$\left(\frac{Z}{L}\right)_{crit} = \frac{1}{1 + \eta} \qquad \text{(condenser end closed)} \qquad (9)$$

where $\eta = \pi_v/\pi_e$.

This position of maximum pressure differential is shown in Figure 2.5A versus $\eta$. For an open-ended design, when the vapor pressure drop is low, and $\eta \sim 0$, then the maximum pressure difference occurs at the evaporator position $Z = L$, as would be expected. When groove vapor pressure drop dominates, then the position of maximum pressure difference tends toward $Z = L/2$ for an open-ended design. Alternatively, when $\eta$ is small for a closed condenser end design, then $Z = L$; for $\eta$ large, the vapor pressure drop dominates and the critical pressure difference occurs at $Z = 0$. To obtain a feeling for the interplay of liquid and vapor pressures in the evaporator, Figure 2.5B shows representative axial groove vapor and liquid pressure changes relative to a constant-pressure vapor core. In the particular case selected, the groove vapor pressure rise and liquid phase pressure drop create a maximum capillary stress at $Z/L = 0.6$.

The points of maximum groove vapor pressure are $Z = L/2$ and $Z = 0$ for open and closed grooves, respectively. If the vapor is in saturated equilibrium with the fluid fillets, then these axial positions will be somewhat higher in temperature than areas where the groove pressure increase is small. However, this pressure difference can never be greater than $2\gamma/r_c$ without exceeding the maximum capillary film pressure and the corresponding temperature rise is negligible for common fluids and operating conditions. It is much more probable that a local temperature increase would be related to meniscus recession, as discussed below.

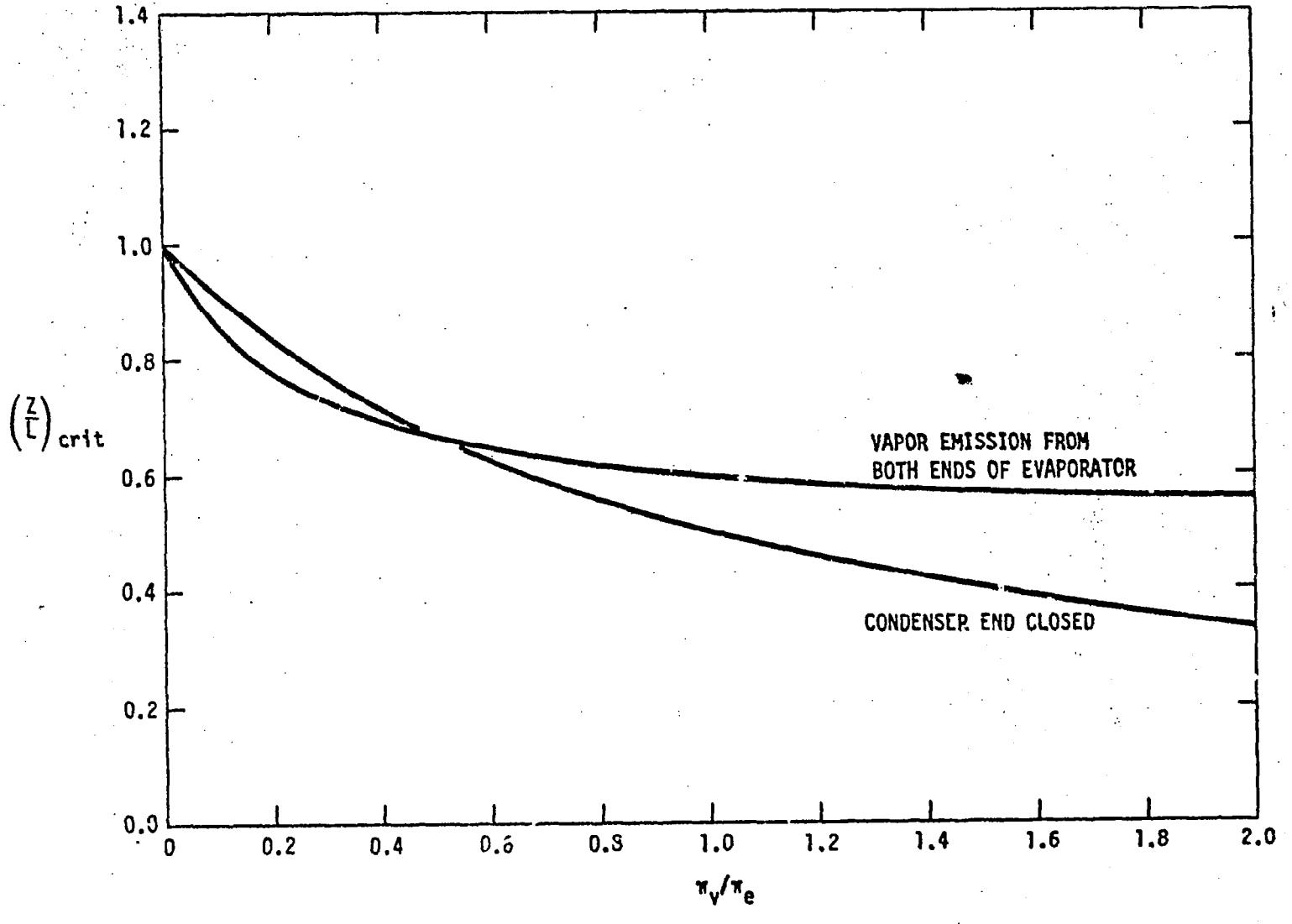


FIGURE 2.5A. THE POSITION OF THE MAXIMUM VAPOR/LIQUID PRESSURE DIFFERENTIAL FOR AXIAL GROOVES

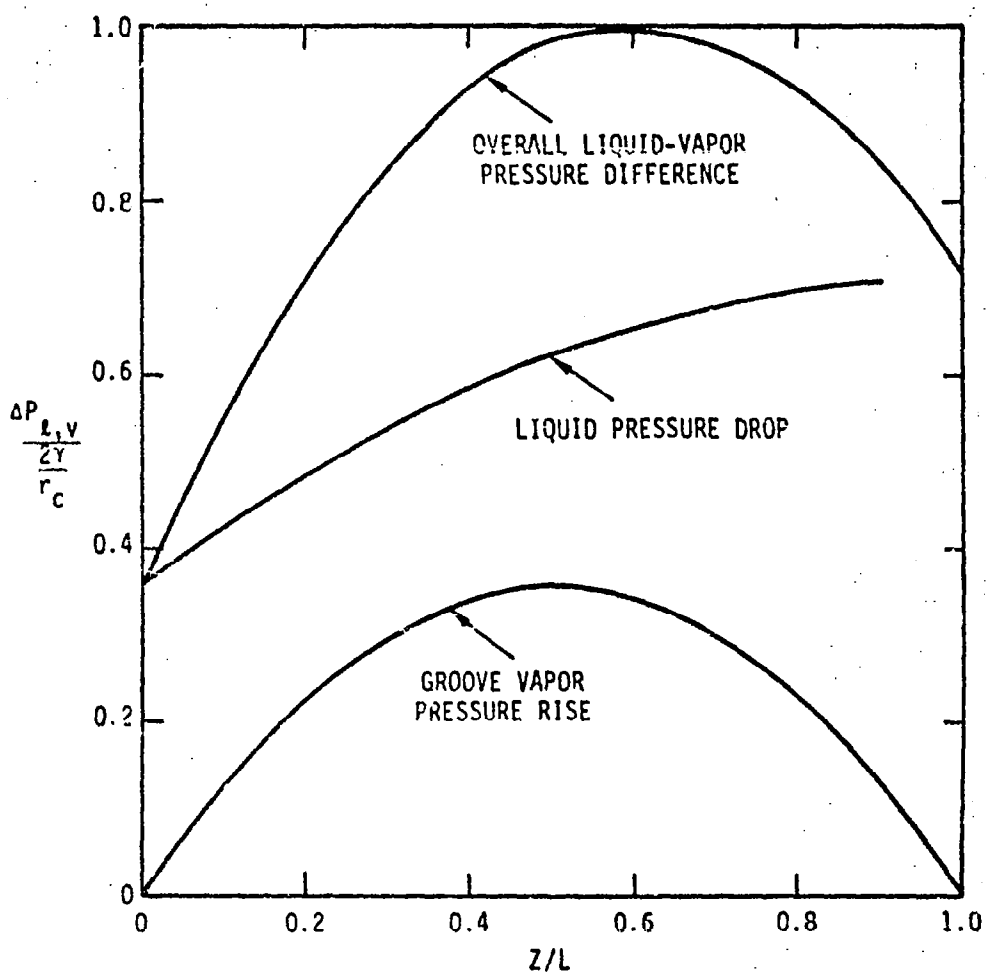


FIGURE 2.5B. PRESSURE CHANGES IN THE LIQUID AND VAPOR PHASES OF AN AXIALLY GROOVED INVERTED MENISCUS EVAPORATOR, RELATIVE TO A CONSTANT-PRESSURE VAPOR CORE. THE SYSTEM IS BEING OPERATED AT THE MAXIMUM HEAT FLUX $Q/Q_m$ = 0.75, AND BURN-OUT OCCURS AT Z/L = 0.6. THE PARAMETER n = 1.0 AND $\pi_e$ = 0.50.

It is straightforward to substitute the expressions for the critical axial position into the sums ($\Delta P_\ell + \Delta P_v$) to obtain the maximum liquid-vapor pressure differences

$$\Delta P_{\ell vm} = \frac{2\gamma}{r_c}\left(\frac{Q}{Q_m}\right)\left[1 + \frac{4\eta^2\pi_e}{1 + 4\eta}\right] \quad \text{(open ends)} \qquad (10)$$

$$\Delta P_{\ell vm} = \frac{2\gamma}{r_c}\left(\frac{Q}{Q_m}\right)\left[1 + \frac{\eta^2\pi_e}{1 + \eta}\right] \quad \text{(condenser end closed)} \qquad (11)$$

Neither expression (10) nor (11) can exceed $2\gamma/r_c$; a higher vapor-liquid pressure differential indicates complete recession of fluid into the circumferential transport wick and local burn-out. Dividing through by $2\gamma/r_c$, expressions result from the maximum fractional pumping power as a function of $\pi_e$ and $\eta$.

$$\frac{Q}{Q_m} \leq 1\Big/\left[1 + \frac{4\eta^2\pi_e}{1 + 4\eta}\right] \quad \text{(open ends)} \qquad (12)$$

$$\frac{Q}{Q_m} \leq 1\Big/\left[1 + \frac{\eta^2\pi_e}{1 + \eta}\right] \quad \text{(condenser end closed)} \qquad (13)$$

The ratio $Q/Q_m$ can be viewed as the reduction in axial transport capacity necessary to prevent vapor blow-through at the axial positions of maximum vapor-liquid pressure difference.

These constraints are shown in Figure 2.6 for the situation that $\pi_e = 1.0$; that is, the liquid pressure drop in the evaporator equals the capillary pumping capacity for $Q = Q_m$. For $\pi_v$ equal to 0.4 of $\pi_e$, the maximum power is reduced by only about 20%. However, for $\eta > 1$, the maximum power is reduced to 60% or less of the theoretical capacity of the axial transport wick.

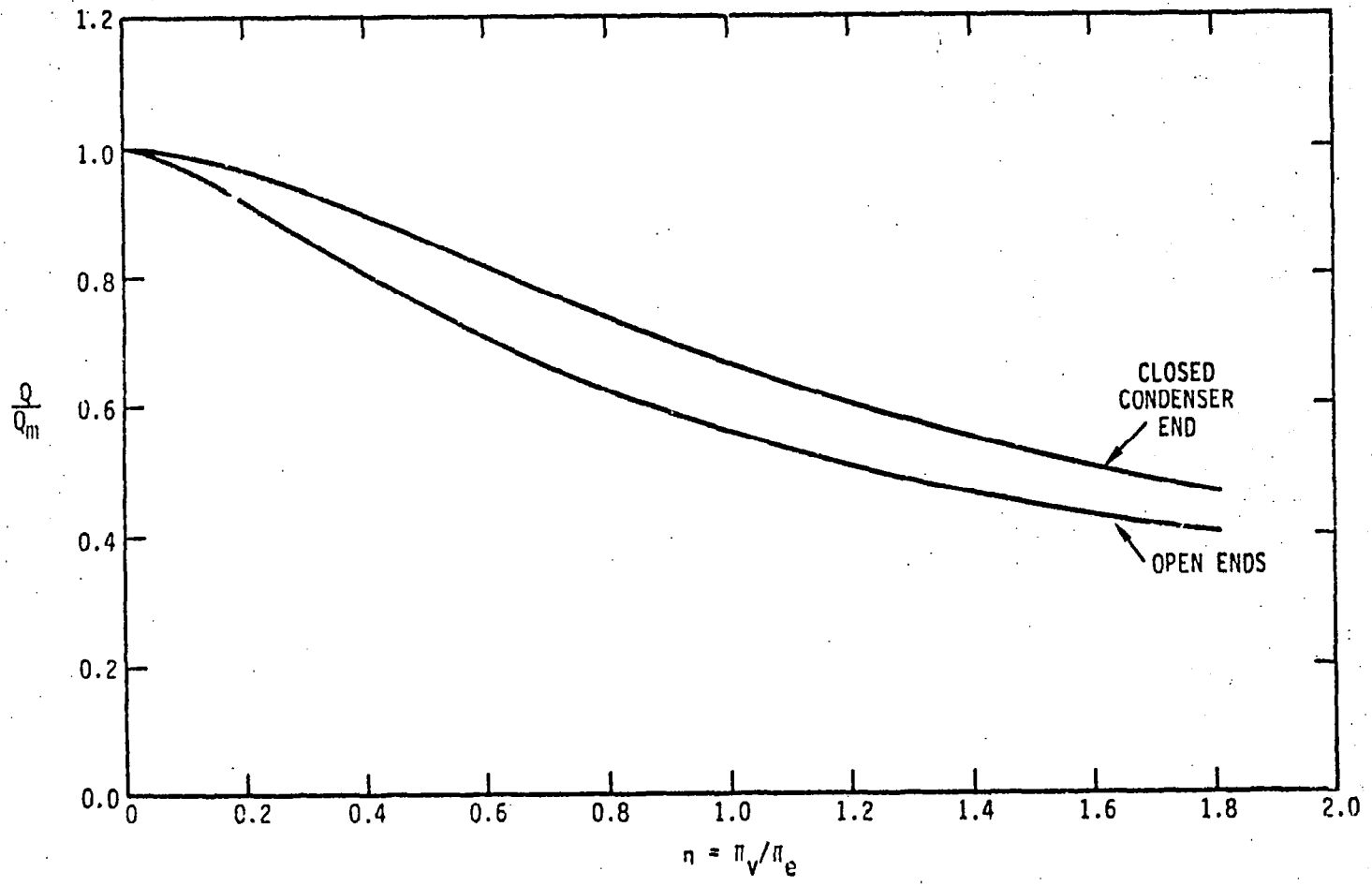


FIGURE 2.6. REDUCTION IN MAXIMUM TRANSPORT CAPACITY AS A FUNCTION OF THE GROOVE VAPOR AND EVAPORATOR LIQUID PRESSURE DROP RATIO, FOR THE WORST-CASE CONDITION $\pi_e = 1.0$

## 2.5 Fluid Recession in a Covered Groove

It is very important to establish at what point an initially primed groove will deprime, since the groove must deprime prior to an inverted meniscus being established.

### Circumferential Grooves

The worst-case criteria for groove deprime is related to fluid recession in the wick. A groove may deprime because of superheat caused by the initially thick fluid film; but, if boiling action does not occur, then the fluid will recede when the liquid-vapor pressure differential exceeds the groove capillary limit, viz.

$$\frac{2\gamma}{R} \leq \Delta P_{\ell} + \Delta P_{v} \tag{14}$$

$$\frac{2\gamma}{R} \leq \Delta P_{\ell}\ (z,\theta_m) \qquad (\Delta P_{v} \approx 0) \tag{15}$$

where R is the groove equivalent radius, and where $\Delta P_{\ell}$ is the overall liquid pressure drop and is recognized to be a function of evaporator axial position, Z, and the vapor emission slit position $\theta_m$ on the heat pipe circumference. Therefore, there is a performance band where the evaporator grooves are only partially operative, depending on axial evaporator position

$$\Delta P_{\ell o \theta_m} < \frac{2\gamma}{R} < \Delta P_{\ell L \theta_m} \qquad \text{(partial deprime between } Z = 0 \text{ and } Z = L\text{)} \tag{16}$$

It is desirable to reduce this band by making the evaporative fluid transport wick of high permeability so that the two vapor-liquid pressure differences are substantially the same. This is also desirable from a fluid transport standpoint.

An operating range can now be defined. On the low side, groove deprime defines a minimum power. On the high side, if groove vapor pressure drop is not excessive, then we have the constraint $\Delta P_{\ell L e_m} = 2\gamma/r_c$. The ratio of maximum to minimum heat transport rate for circumferential grooves is then approximately

$$\frac{Q_{max}}{Q_{min}} \cong \frac{R}{r_c} \tag{17}$$

It is favorable from this standpoint to maintain $r_c$ as small as possible to gain the largest heat transfer band.

Axial Grooves

Whether grooves extend circumferentially or axially, the primary vapor-liquid pressure constraints are the same, with one possible exception. The maximum heat transport rate may be reduced as discussed in Section 2.3, and shown in Figure 2.6, because of groove vapor pressure buildup attributable to a considerably greater covered length. It has not been discussed previously, but this could be overcome by systematic circumferential vapor release slots along the evaporator. However, this type of wick would be difficult to fabricate.

Groove Reprime

An inverted meniscus design can display hysteresis in groove deprime and subsequent reprime. On the first power increase, the grooves will deprime as discussed in the preceding paragraphs. However, if the grooves are completely

deprimed and then the heat transport rate is decreased, the grooves may not reprime except at a much lower power level than that given by equation (15). Once the grooves are deprimed completely, the reprime proceeds with only a one-dimensional fillet. Therefore, disregarding vapor pressure buildup in the grooves, the reprime constraint is

$$\frac{\gamma}{R} \leq \Delta P_{\ell} \tag{18}$$

for the case of both ends open for axial grooves, or for all cases with circumferential grooves.

## 3. EXPERIMENTAL TESTING

### 3.1 Experimental Vehicle Description

To test relative performance of open-faced grooves and the inverted meniscus evaporator, a heat pipe was constructed with a short cylindrical evaporator section as detailed in Figure 3.1. The active evaporator surface is 3.81 cm long and 1.27 cm in diameter for a total internal surface area of 15.20 $cm^2$. The surface is spirally grooved with 25.0 grooves/cm of the characteristic cross section shown in Figure 3.2

In Figure 3.1, one end of the cylindrical evaporator is closed with a circular glass port and O-ring seal. The opposite end couples via an O-ring seal end flange to a thin-walled adiabatic section 30 cm long. A 15 cm condenser section is sealed by another O-ring flange. This end flange has a penetration for charging as well as a penetration for a 0.125-inch-diameter tube of 30 cm length. This tube is sealed off and used as a thermocouple well to monitor vapor core temperature. In addition to a thermal well in the condenser end cap, the heat pipe is thermally monitored with 12 thermocouples

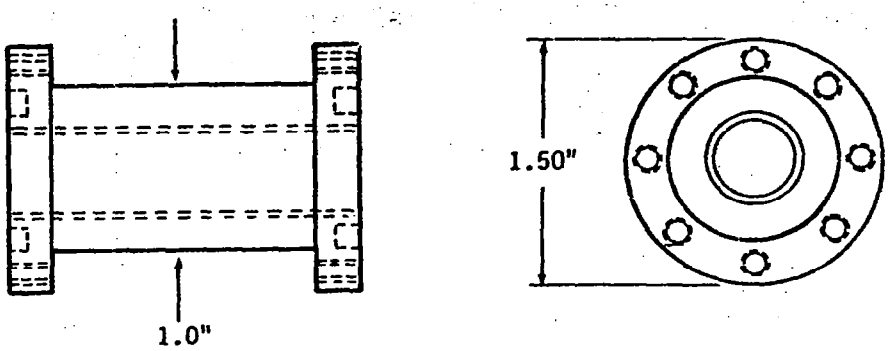


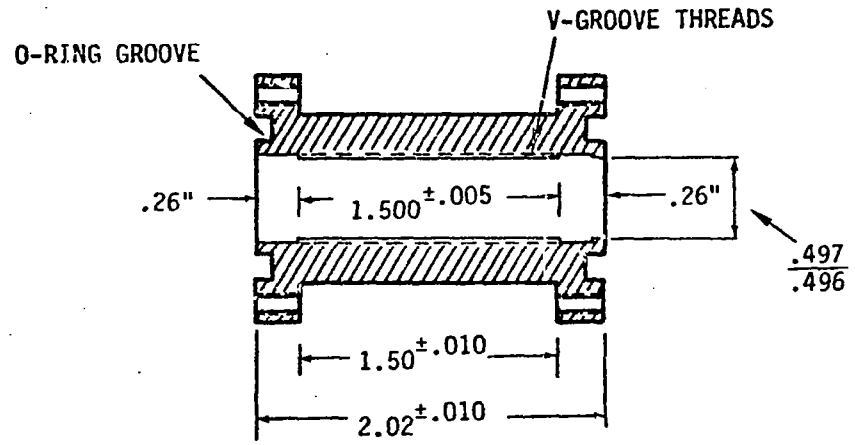


FIGURE 3.1. EVAPORATOR ASSEMBLY FOR INVERTED MENISCUS TESTING IN CYLINDRICAL GEOMETRY. ALL DIMENSIONS IN INCHES (1. INCH = 2.54 CM).

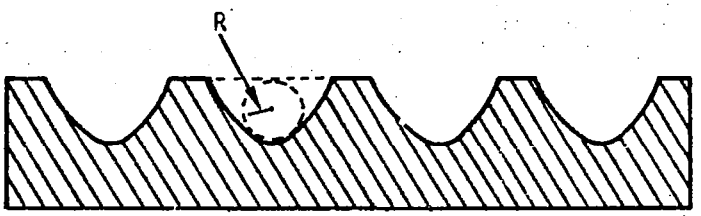


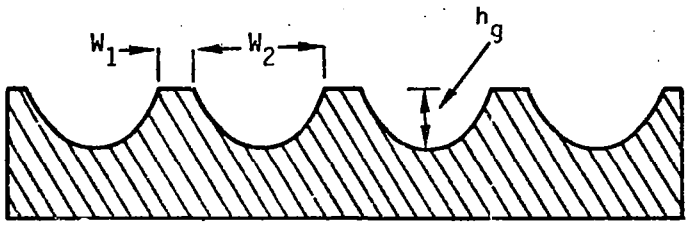


| CHARACTERISTIC DIMENSION | VALUE | |
|---|---|---|
| | WINDOW END | ADIABATIC END |
| $W_1$ | 0.00895 CM | 0.00726 CM |
| $W_2$ | 0.0310 | 0.0327 |
| $h_g$ | 0.0167 ± 0.0006 | 0.0155 ± 0.0005 |
| R | 0.0083 | 0.0072 |
| Wetted Perimeter | 0.048 CM | 0.050 CM |
| Cross-Sectional Area | $2.9(10^{-4})CM^2$ | $2.9(10^{-4})CM^2$ |

FIGURE 3.2. GROOVE CROSS SECTIONS TAKEN FROM WAX CASTINGS SHOWING GROOVE DETAIL AT BOTH ENDS OF EVAPORATOR

inserted radially to a depth of 0.46 cm in the 0.62 cm evaporator wall. Eight of the thermocouples are inserted at 90° intervals in proximity to the two end flanges, while the remaining four thermocouples are spaced at 90° internals in the center of the evaporator.

The heater is an Inconel ribbon of 0.16 cm width wrapped on a single layer of 0.009 cm thick Teflon film. A thin layer of DC-340 applied prior to heater winding assures adequate thermal contact of the ribbon with the Teflon film. The ribbon heater assembly and thermocouple leads are potted in a flexible silicone blanket such that the blanket has an O.D. identical to the O.D. of the evaporator end flanges. The silicone material serves to stabilize heater ribbons and thermocouple leads against relative movement, which is an important variable at high radial flux densities. If a heater ribbon contacts a thermocouple lead, that thermocouple location can read erroneously high.

At a maximum heat flux of 100 watts or 6.5 watts/$cm^2$ (42 W/$in.^2$), the temperature rise of the ribbon heater above the aluminum wall is calculated to be 25.5°C. Under these maximum temperature conditions, if all parts are covered with the thermal insulation package, which is 2.54 cm in thickness and has a thermal conductivity 0.36 ($10^{-3}$) W/cm °K (Johns Manville Aerotube™), then the insulation conductance is calculated as 0.017 W/°K, neglecting heat losses from the end window. In actual tests, the lumped conductance of the experimental vehicle to ambient was measured to be 0.060 W/°K and, in most cases, this conductance affected the tests negligibly. Laboratory ambient was 23 to 25°C.

A detail of the circumferential transport wicking for the inverted meniscus is presented in Figure 3.3. In this cross section, six layers of 400-mesh 304 stainless screen are in intimate contact with a spirally grooved

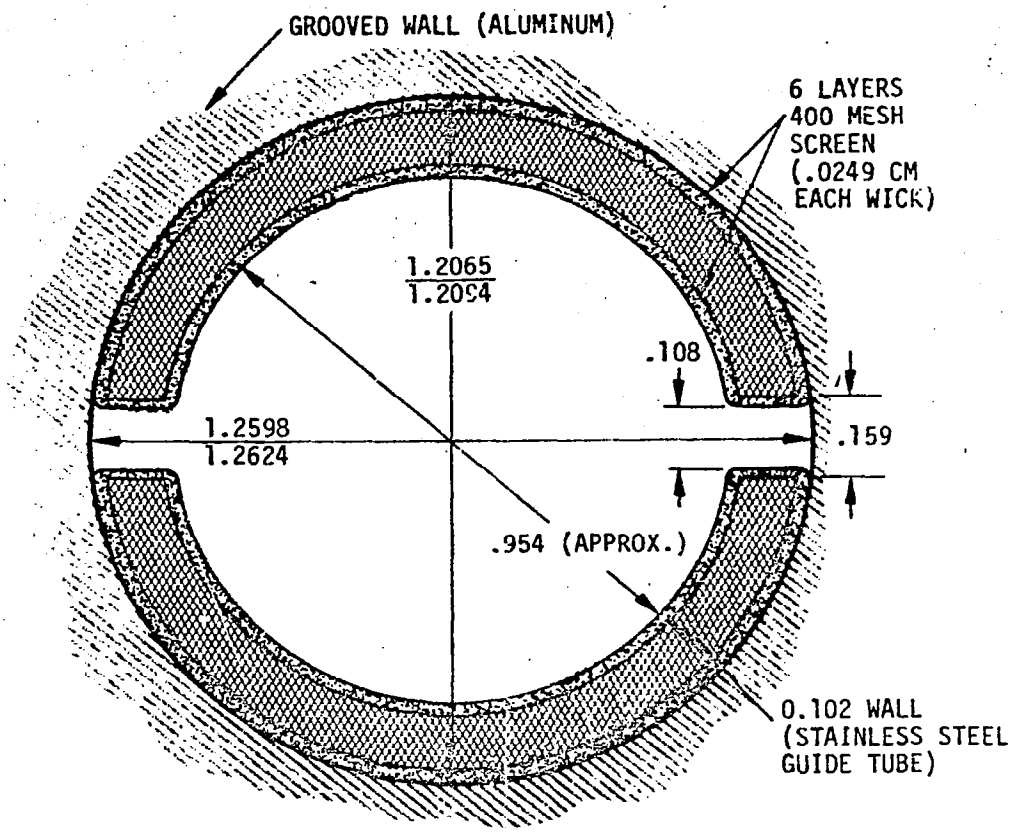


FIGURE 3.3. SECTIONAL VIEW OF INVERTED MENISCUS HEAT PIPE EVAPORATOR SHOWING DETAILS OF CIRCUMFERENTIAL EVAPORATIVE TRANSPORT WICK. NOTE STAINLESS GUIDE TUBE FOR ACCURATELY PLACING CIRCUMFERENTIAL WICK IN CONTACT WITH GROOVED WALL. TOTAL HEAT TRANSFER AREA IS 15.2 $CM^2$. ALL DIMENSIONS IN CM.

internal diameter. A close-fitting guide tube holds the screen tightly against the wall. The tube has been slit partially down its length on opposite sides so that the screens may be drawn tightly over the tube and inserted through the slits to be spot-welded to the inner surface of the guide tube. The six layers of screen are allowed to overlap on the inside guide tube diameter so as to provide an area for the axial wick to transfer fluid to the circumferential wick. As assembled, the screen-affected diameter is perhaps 0.0025 cm larger than the I.D. of the grooved tube, but inherent looseness in a multilayer wick allows the guide tube and wick to be inserted. Segmentation of the circumferential wick and passage through a slit as shown also allows excess wick to be relieved into the open area of the slit when the device is assembled so long as the slit is not completely blocked off. Each vapor release slit is approximately 0.108 cm wide, and both together account for 5.4% of the total area. This area is not subtracted when calculating the heat transfer coefficient, and values given are therefore overall figures for the total available area.

Figure 3.4 presents the configuration used for testing open grooves with a pedestal artery axial transport wick. The artery has a 0.159 inside diameter and rests on a 0.254 cm stem. For testing of the evaporator with open grooves, the upper pedestal was increased in length by about 0.3 cm to accommodate the larger internal diameter. Prior to thermal testing, the artery was tested for static deprime height to establish the largest pore size, and the deprime height was very close to that expected for 400-mesh square-weave stainless screen. The capacity of the artery, when primed, is much higher than can be sustained by open grooves.

To ensure adequate fluid transport for inverted meniscus tests, the axial wick shown in Figure 3.5 was used.

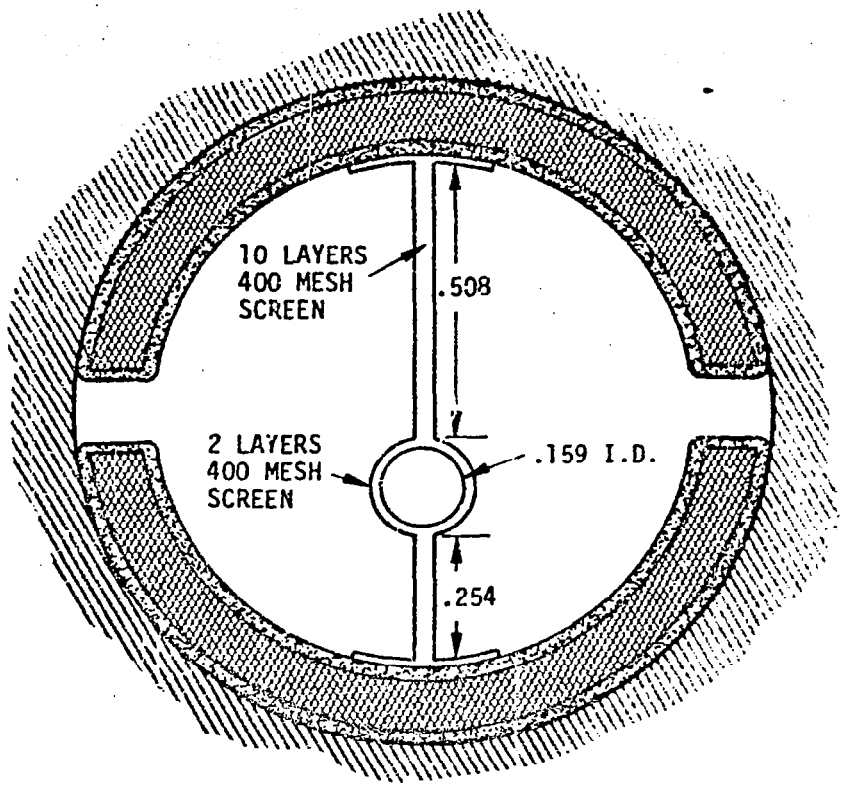


FIGURE 3.4. SECTIONAL VIEW OF INVERTED MENISCUS HEAT PIPE EVAPORATOR WHEN USED WITH .159 CM DIA. PEDESTAL ARTERY AXIAL TRANSPORT WICK. BOTH PEDESTALS HAVE BEEN REMOVED IN ADIABATIC SECTION. ALL DIMENSIONS IN CM.

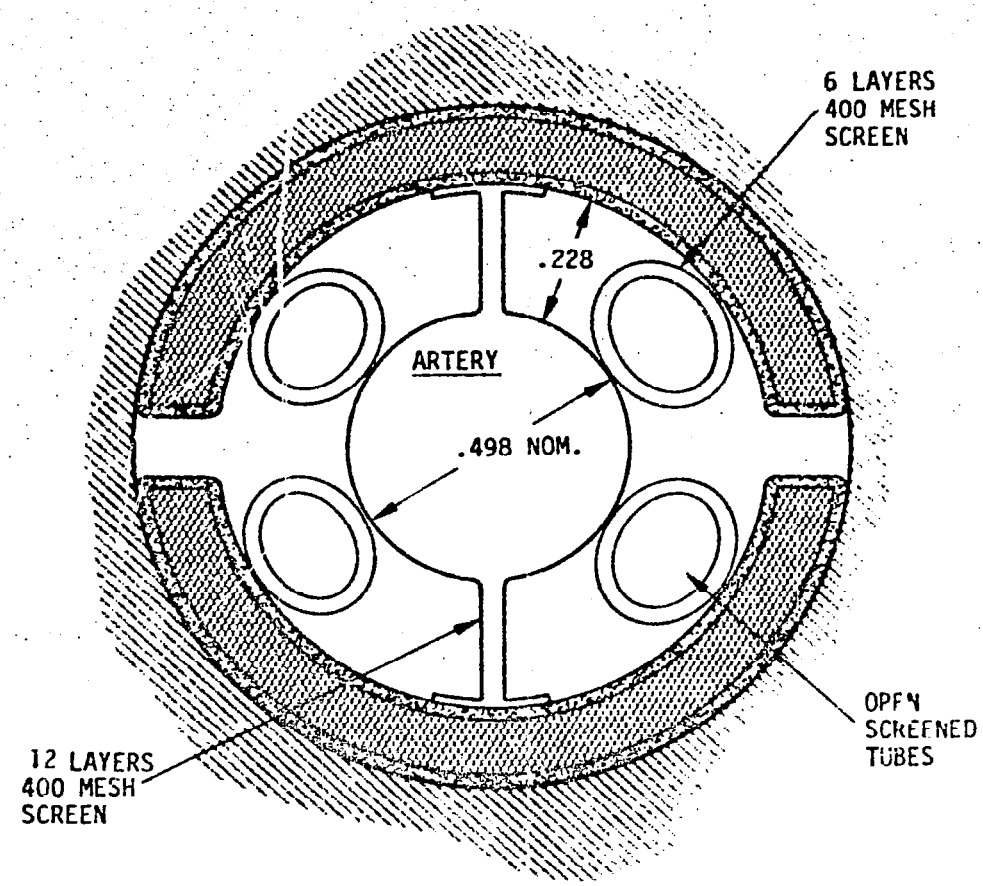


FIGURE 3.5. SECTIONAL VIEW OF INVERTED MENISCUS HEAT PIPE EVAPORATOR WHEN USED WITH MULTIPLE-TUBE ARTERY AND RADIAL TRANSPORT WICKS COMPOSED OF OPEN-ENDED SCREEN TUBES IN COMPRESSION BETWEEN ARTERY AND CIRCUMFERENTIAL WICK

The central artery consisted of 19 screened single-layer tubes of 0.079 cm outside diameter fitted into an outer wrap of 0.498 cm diameter. All screens used were 400-mesh square-weave stainless steel. The pedestal stems, which were only used in the evaporator and condenser, were of 12 layers and 4 layers, respectively.

3.2 Experimental Technique/Test Results

Prior to testing, the heat pipe was flooded with ammonia or R-11 and allowed to remain stagnant for a period of 1/2 to 1 hour to vent internal gas occlusions. The heat pipe was then elevated to an adverse tilt of 3.0 cm and fluid removed until a fluid leg of only 5 cm or less was apparent with the vapor probe in the far condenser end. At this point, the heat pipe was considered primed and charged. Because of the fluid leg remaining in the condenser, under level conditions and up to an adverse tilt of approximately 0.7 cm, it was possible for a small pool to exist in the heat pipe up to the evaporator, assisting the artery in axial fluid transport. Beyond approximately 1.0 cm, the pool has receded away from actual contact with the evaporator. When a pool definitely is present in the evaporator, boiling generally occurs. The [illegible] in the figures to be presented the temperature differences at zero elevation may be low because of nucleate boiling.

The condenser liquid leg was easily observed in ammonia testing, but somewhat more difficult to observe with R-11. It appears that R-11 may have similar boiling-point refrigerants as significant impurities since the temperature gradient in the condenser extended over a considerable distance; a long gas front is characteristic of a multicomponent system. Figure 3.6 shows the

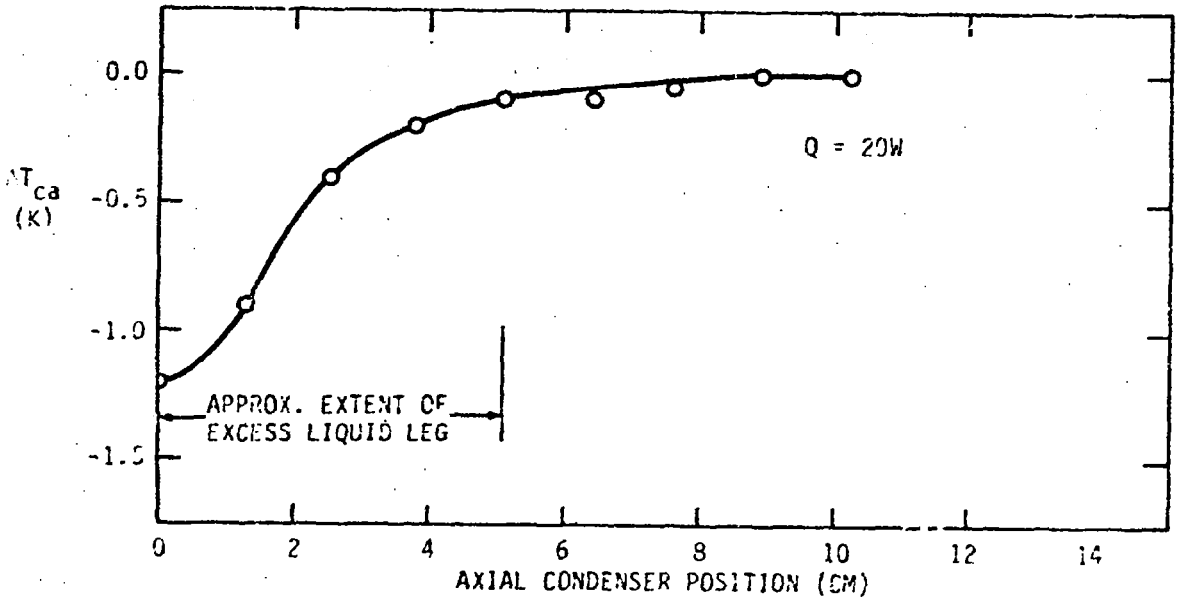


FIGURE 3.6. TEMPERATURE PROFILE IN CONDENSER VAPOR CORE SHOWING EXCESS AMMONIA FLUID COLLECTION AT EXTREME CONDENSER END WHEN HEAT PIPE WAS TILTED 3.0 CM. TEMPERATURES SHOWN RELATIVE TO ADIABATIC VAPOR TEMPERATURE

liquid leg existing during ammonia performance runs. This data was taken using the thermocouple probe tube in the condenser. The liquid leg is about 5 cm long at a 3 cm external tilt, and has negligible effect on performance, as shown by data taken at various tilts in Figure 3.6.

Figures 3.7 and 3.8 present open-grooved heat transfer data for ammonia and R-11 at a nominal temperature of 30°C. As can be seen, the heat transfer coefficient is quite sensitive to adverse tilt in each case. As mentioned earlier, up to an external tilt of about 0.7 cm, a pool extends into the evaporator and boiling is visible at lower heat fluxes. At higher heat fluxes, the demand for liquid is such that the pool recedes and wick pumping dominates in the evaporator (although a pool still will exist in the adiabatic). Therefore, a performance band from 0.0 to 1.46 cm has been selected as typical of operating conditions in order to characterize open-groove heat transfer in a condition close to zero-g, and yet compensate for possible pool boiling effects. The zero-g low-power heat transfer coefficients are less than or equal to the values for 0.0 cm tilt (0.79 and 0.54 $W/cm^2$ °K for ammonia and R-11, respectively) and greater than the values for 1.46 cm tilt (0.44 and 0.23 $W/cm^2$ °K for ammonia and R-11, respectively).

Figures 3.9 and 3.10 present data for the inverted meniscus wick. Figure 3.10 also shows, for ammonia, the increase in heat flux obtainable with this concept beyond open grooves. For open grooves, a heat flux density of about 4 $W/cm^2$ was obtained while a heat flux density of 20 $W/cm^2$ was achieved with the inverted meniscus. For R-11, flux densities on the order of 1.5 and 5 $W/cm^2$ were achieved with open grooves and the inverted meniscus, respectively. A higher watt density for ammonia could have been achieved with the inverted

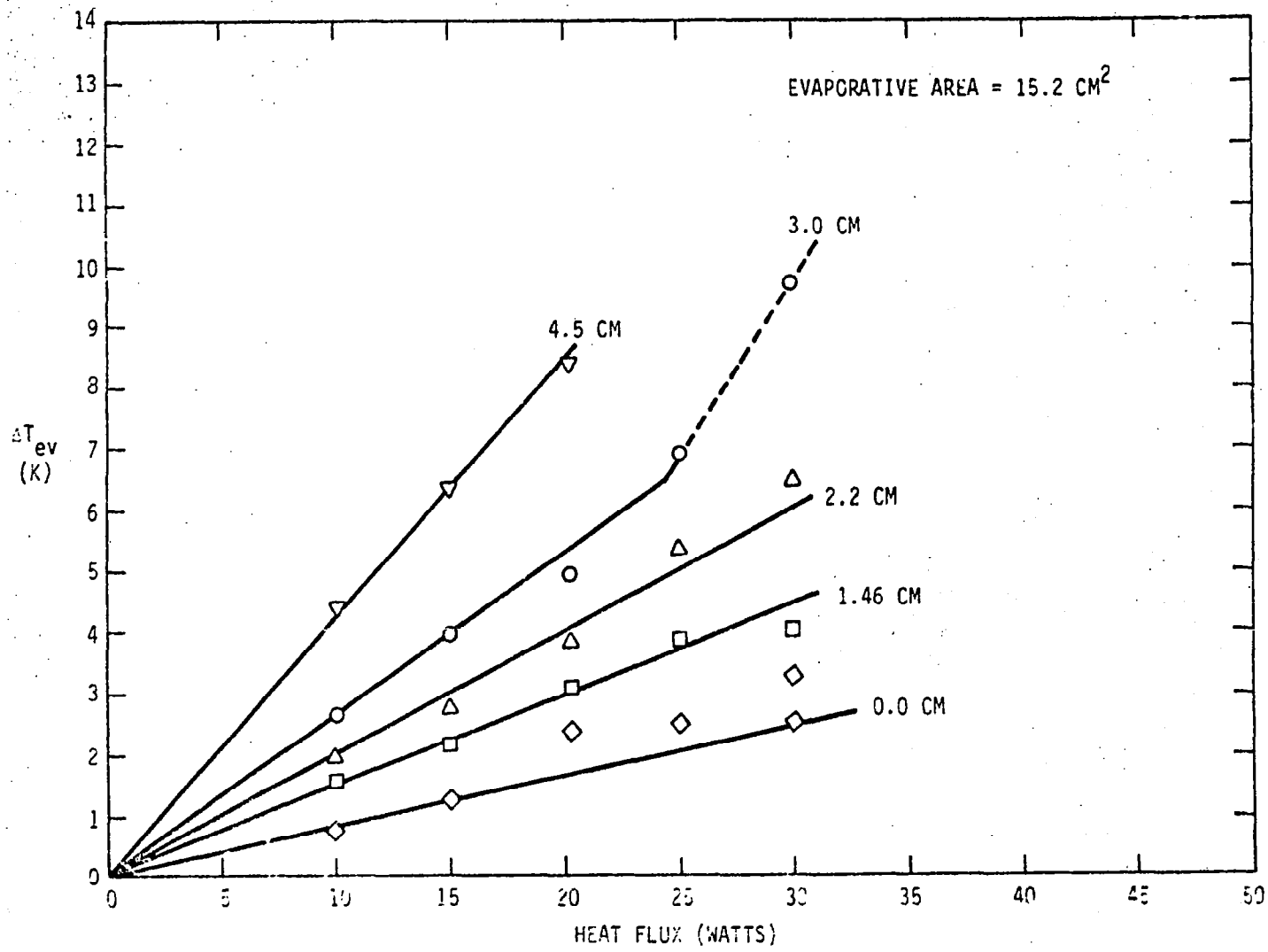


FIGURE 3.7. PERFORMANCE BEHAVIOR OF OPEN GROOVES WITH AMMONIA AT 30 ± 10°C FOR VARIOUS EXTERNAL ADVERSE TILTS. PEDESTAL ARTERY AXIAL TRANSPORT WICK

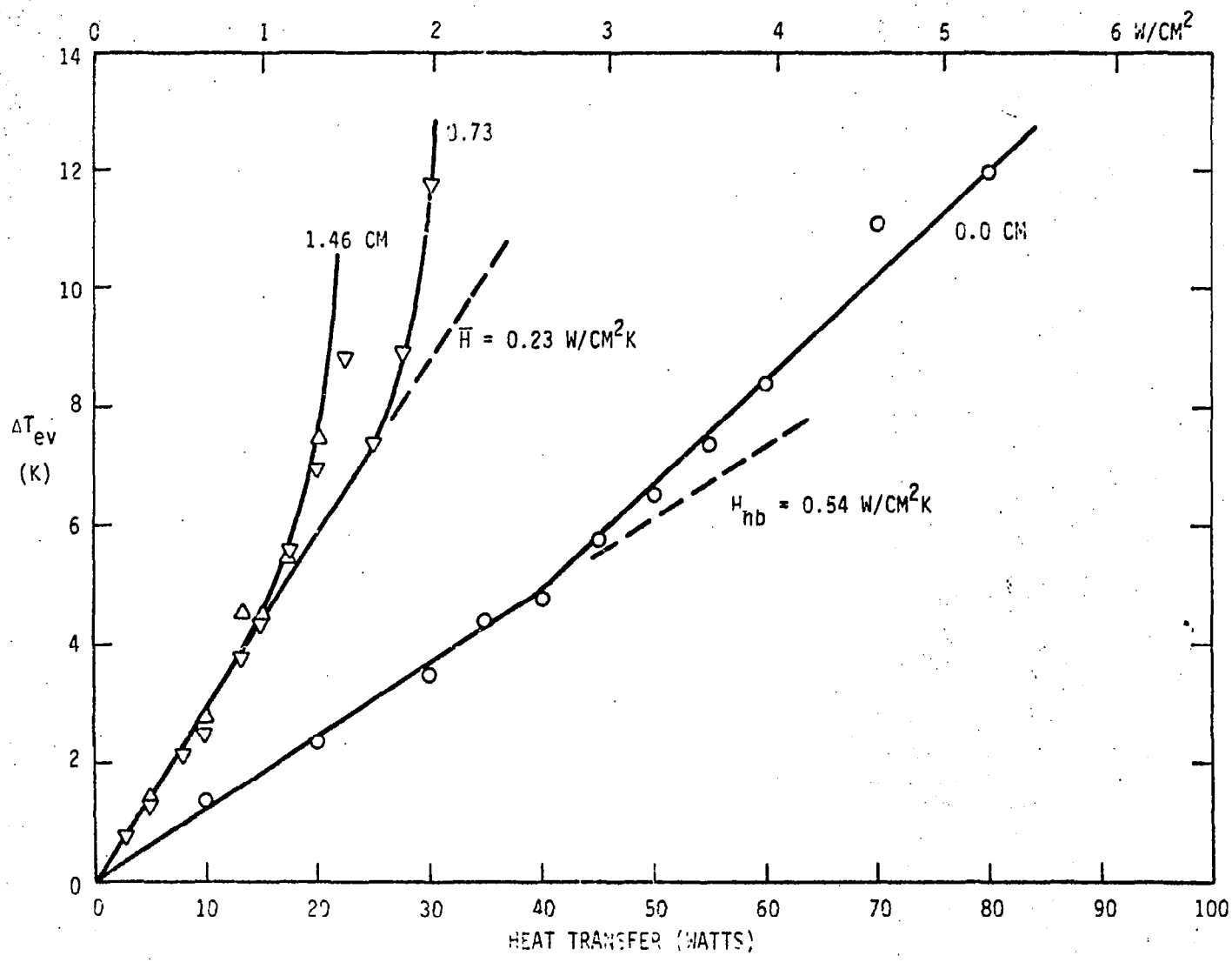


FIGURE 3.8. PERFORMANCE OF OPEN GROOVES WITH R-11 AT 25 ± 5°C FOR VARIOUS EXTERNAL ADVERSE TILTS. MULTIPLE-TUBE ARTERY AXIAL TRANSPORT WICK. RADIAL SCREEN TUBES REMOVED. AT HORIZONTAL ELEVATION, VIGOROUS NUCLEATE BOILING IS APPARENT IN PUDDLE.

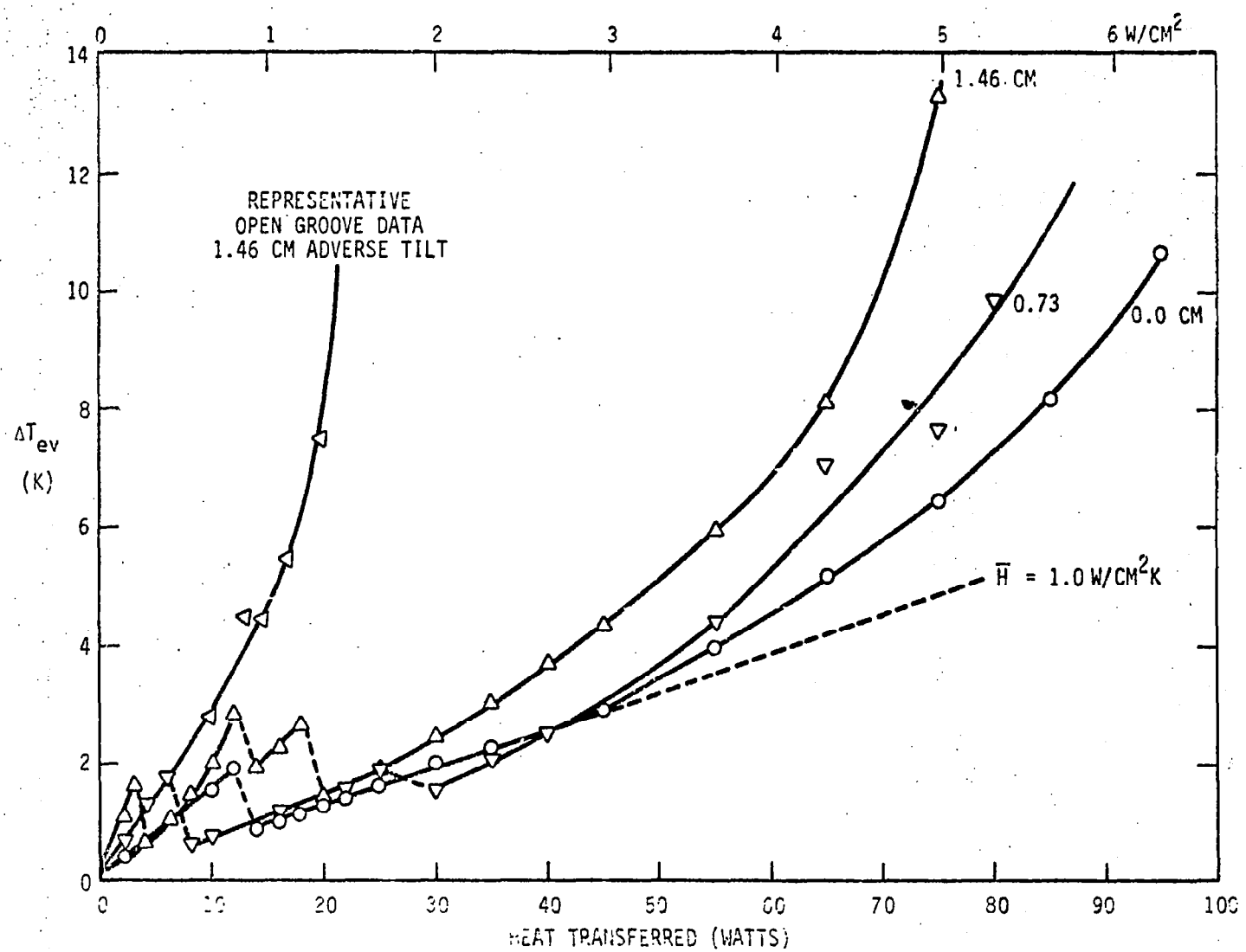


FIGURE 3.9. PERFORMANCE BEHAVIOR OF INVERTED MENISCUS WICK WITH R-11. AXIAL WICK IS MULTIPLE-TUBE ARTERY. NOTE GROOVE DEPRIME PHENOMENA AT LOWER POWER.

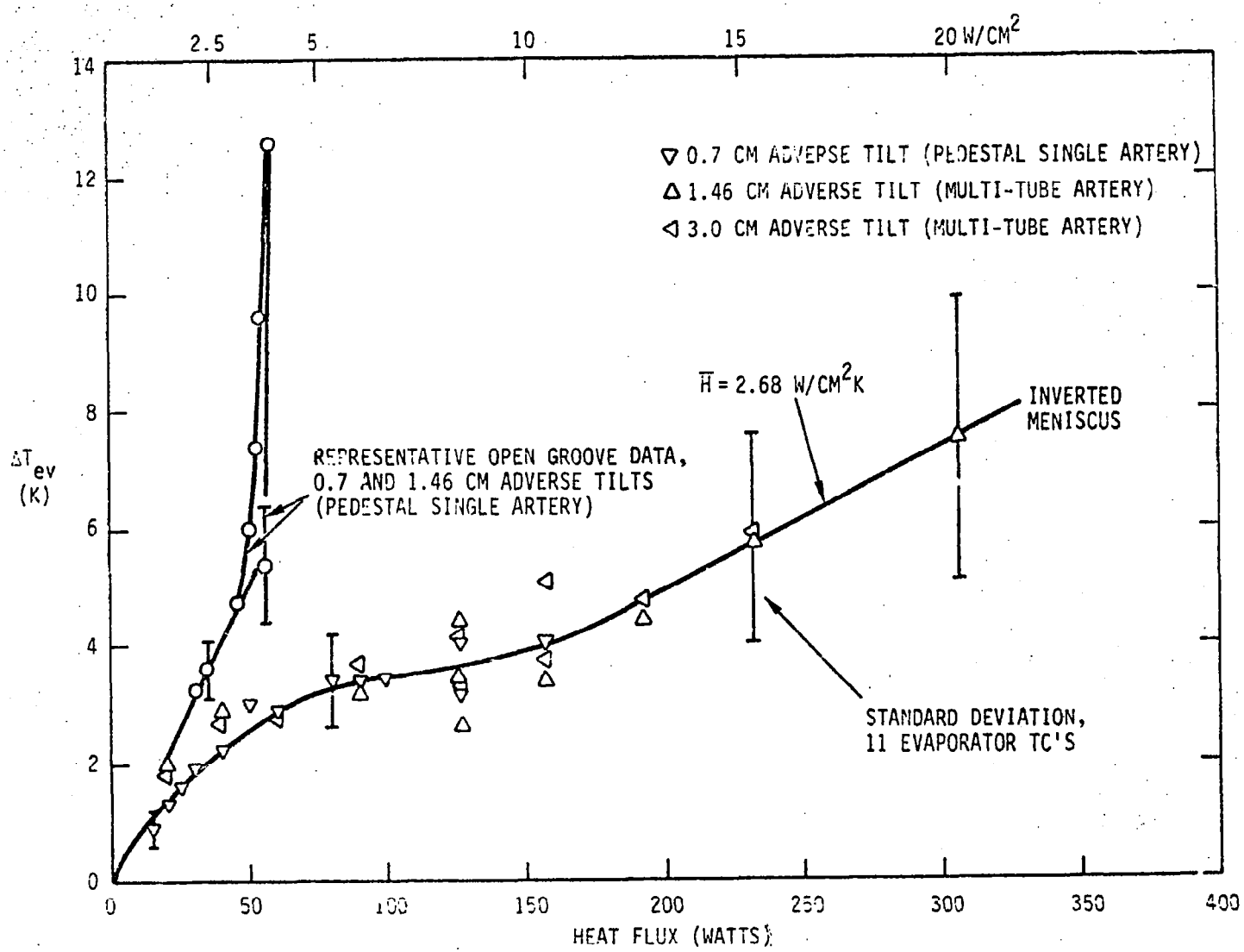


FIGURE 3.10. COMPARISON OF OPEN GROOVE AND INVERTED MENISCUS PERFORMANCE FOR AMMONIA. AT 0.7 CM ADVERSE TILT, OR LESS, BOTH DESIGNS USE FLUID RETURN VIA INTERNAL PUDDLING IN PARALLEL WITH THE AXIAL WICK. EVAPORATOR AREA = 15.2 CM$^2$.

meniscus but electrical demand exceeded the available power supply capacity. Maximum heat transfer coefficients of 1.0 and 2.68 $W/cm^2°K$ have been measured for R-11 and ammonia with the inverted meniscus.

Because of the extensive and impenetrable surface covering, groove boiling was the common mode for initiation of inverted meniscus behavior. In Figure 3.9 at low watt density, erratic behavior is seen which may be attributable to groove depriming. No erratic precursors were seen with ammonia. At low flux levels, both fluids also exhibited a spitting action in which liquid droplets were ejected from the axial vapor release slot. At higher heat fluxes (on the order of 5 $W/cm^2$ for ammonia and 1 $W/cm^2$ for R-11), this behavior disappeared and groove flow dynamics stabilized.

Large standard temperature deviations shown in Figure 3.10 at high heat flux are primarily attributable to unusually high temperatures at only 2 out of the 11 recording evaporator thermocouples. Temperature gradients at high flux density are shown in Figures 3.11 and 3.12 as a function of evaporator position. At each 90° position, there are three thermocouples along the evaporator length: one at each end of the evaporator and a third at the mid-point. The sketch in each figure shows thermocouple orientation with respect to the covering wick; i.e., positions $P_1$ and $P_3$ are points farthest from the axial vapor slits while $P_2$ and $P_4$ are immediately over the slit. The thermocouple at position $P_1$ at the window-end of the evaporator malfunctioned and is not included.

At both power levels shown, the center positions over the vapor slits have significantly higher $\Delta T$. It has not been possible to explain this behavior. It is possible that heaters may be closer to thermocouple lead-in wire, or

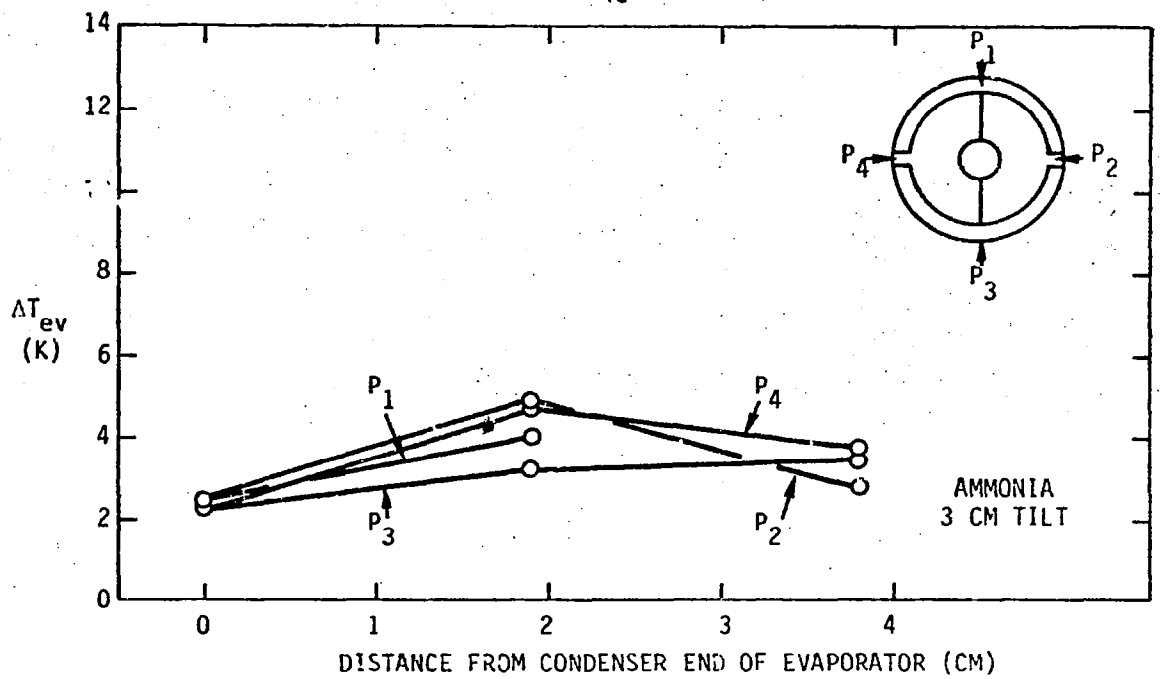


FIGURE 3.11. EVAPORATOR TEMPERATURE GRADIENTS ALONG VARIOUS AXIAL LINES FOR Q = 127W.(8.3 W/CM$^2$)

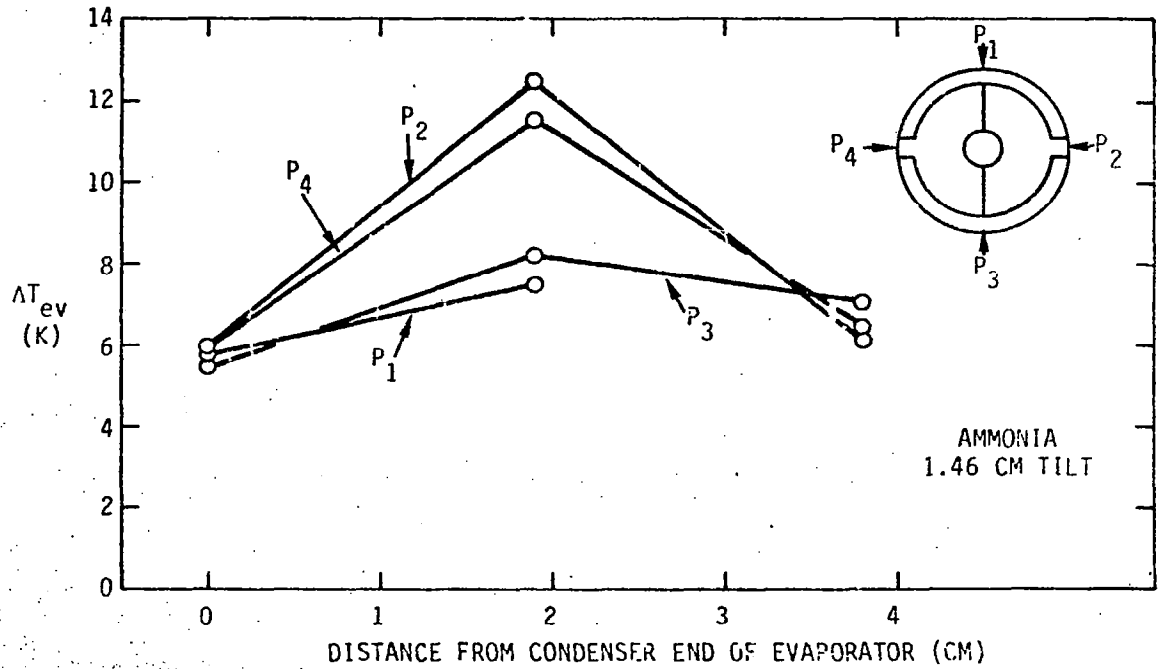


FIGURE 3.12. EVAPORATOR TEMPERATURE GRADIENTS ALONG VARIOUS AXIAL LINES FOR Q = 306W. (20 W/CM$^2$)

screen fit-up could be altered in these areas. Since the heat loss at each end by parasitics is negligible, there should be no inherent axial gradient peaking at the center. For example, if the lack of screen at $P_2$ and $P_4$ were to create a local temperature rise, this rise should be relatively uniform over the evaporator length.

Figure 3.13 shows maximum heat flux versus external adverse tilt for ammonia and both evaporative surfaces. Very large differences in performances are apparent. The inverted meniscus evaporator has a maximum heat flux at least four times that of the open grooves and a maximum external adverse tilt at least twice that for the open grooves. Predicted performance shown in Figure 3.13 is discussed in the following section 3.3, Data Interpretation.

## 3.3 Data Interpretation

Figure 3.13 shows calculated transport limits as well as experimental data. Performance of the open-grooved evaporator was calculated using standard methods for estimating pressure drop in the various stems and artery. For calculating open groove pressure drop, an approximate hydraulic model was used of the form

$$\Delta P_{\ell g} = \left(\frac{M_a \mu_f}{\rho_f H_{fg}}\right) \frac{\ell_e Q_g}{K_{pg} \langle A_g \rangle} \qquad (\text{dynes/cm}^2) \qquad (19)$$

where $\ell_e$ is the effective length of a single groove and $Q_g$ is the single-groove heat rejection rate. The average fluid cross-sectional area is $\langle A_g \rangle$, and $K_{pg}$ is the fillet permeability. If $K_{pg}$ is calculated from the expression

$$K_{pg} = \frac{r_h^2}{8} \qquad (\text{cm}^2) \qquad (20)$$

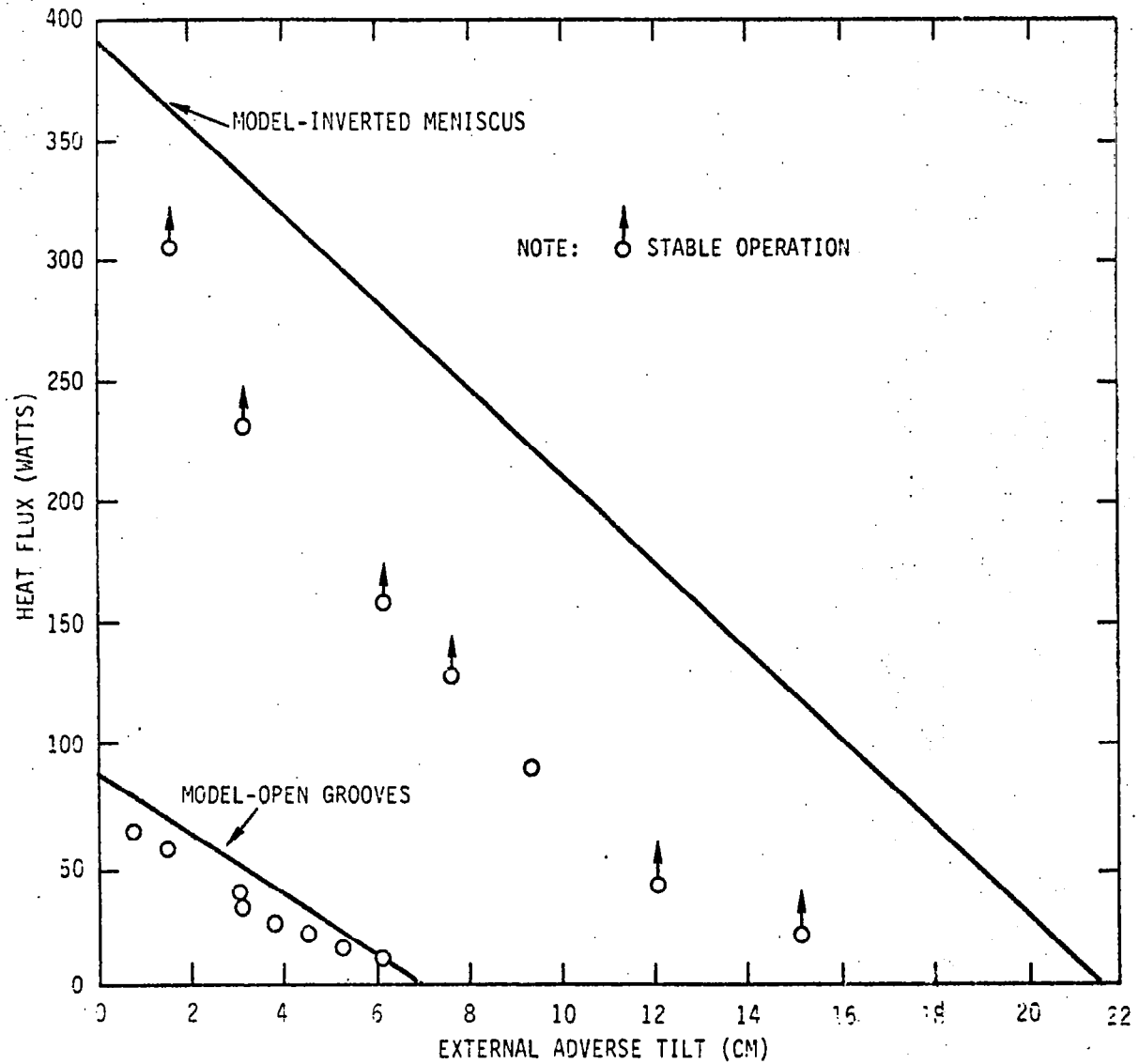


FIGURE 3.13. HEAT FLUX VERSUS ADVERSE TILT FOR AMMONIA AT 30 ± 5°C USING BOTH OPEN GROOVES AND INVERTED MENISCUS EVAPORATOR. DATA FOR OPEN GROOVES ARE ALL BURN-OUT POINTS, BUT ALL MEASUREMENTS WITH EXCEPTION OF Q = 90 W ARE STABLE OPERATING POINTS FOR INVERTED MENISCUS WICK.

where $r_h$ is the fillet hydraulic radius, and if the average fluid cross section is taken as one-half the groove cross section, then the fluid pressure drop in a groove is given as

$$\Delta P_{\ell g} = \frac{8}{\pi} \frac{M_a \mu_f}{\rho_f H_{fg}} \left(\frac{P^2}{A^3}\right) \frac{x^2 Q}{NDL} \qquad (\text{dynes/cm}^2) \qquad (21)$$

in this representation $\ell_e$ has been assumed to be one-half x, the total circumferential groove length from a stem to the minimum fluid pressure position. This representation for effective length assumes a uniform circumferential evaporation rate. The wetted perimeter and cross-sectional area at the window end of the heat pipe are given with Figure 3.2. Other pertinent system properties are tabulated in Table 3.1. The critical circumferential position for burn-out of this double-stem artery is very close to the top of the heat pipe, and was calculated by varying x to maximize the pressure drop relative to the axial transport wick.

The one-dimensional groove radius, R, used for calculating surface tension pumping pressure, was selected on the basis of the groove inscribed circle shown in Figure 3.2.

The maximum prime-height for the open-groove surface is correlated by

$$\rho_f g h_m = \frac{2\gamma}{R} \qquad (22)$$

where $h_m$ is the total adverse elevation and R is the inscribed circle discussed previously. At high adverse elevations, the heat pipe will operate until the liquid plug formed by contact of the radial wick and grooves is deprimed. This means that at higher elevations the grooves may actually be partially dry as in the tests shown in Figures 3.6 and 3.7. This may explain the significant degradation in heat transfer with adverse tilt.

TABLE 3.1. SYSTEM PARAMETERS USED IN CALCULATING LIQUID PRESSURE DROPS AT 30°C FOR AMMONIA

| Parameter | Value |
|---|---|
| Surface tension | 19 dynes/cm |
| Fluid viscosity | 0.13 cp |
| Fluid density | 0.593 g/cc |
| Latent heat | 19,450 Joules/g-mole |
| Screen permeability | 6.50 ($10^{-7}$) $cm^2$ |
| Screen thickness | 0.00419 cm per layer |
| N | 25 grooves/cm |
| L | 3.81 cm |
| R | 0.0083 cm |
| Effective heat pipe length | 54.6 cm |
| $r_c$ (400 mesh) | 0.00318 cm |
| Vapor viscosity | 0.0102 cp |

Multiple-tube artery performance was correlated with the model discussed in reference 7. Since fluid transport is independent of groove size with the inverted meniscus, the characteristic pore size of 400-mesh screen establishes maximum capillary pumping. Note that the operating points for inverted meniscus testing shown in Figure 3.13 are not burn-out points. Operation in the inverted meniscus mode was demonstrated over a significant portion of the thermal performance envelope.

A maximum heat flux density of 20 $W/cm^2$ was achieved with ammonia and about 5 $W/cm^2$ with R-11. Using the groove geometry found in Figure 3.2 and analytical expressions in Section 2, the vapor-phase pressure difference created by circumferential groove vapor flow was calculated. This pressure difference contributes to fluid recession into the wicking. At a flux density of 20 $W/cm^2$, calculations show approximately 21% to 36% of the driving capillary pressure is balanced by a groove vapor flow pressure differential. At 20 watts per $cm^2$ it has also been calculated that the axial and circumferential liquid pressure drop accounts for about 78% of the capillary driving pressure. Therefore, the wicking in this test was being stressed to approximately theoretical capacity at 20 $W/cm^2$. In the case of R-11 at 30°C, a maximum heat flux of 6.7 to 11.6 $W/cm^2$ is indicated when all capillary pressure supports the groove vapor differential. This is in qualitative agreement with the rise in evaporator $\Delta T$ seen for flux densities greater than 5 $W/cm^2$.

## 4. SUMMARY

A brief outline of measured heat transfer coefficients is given in Table 4.1. The inverted meniscus evaporator has been shown to markedly increase radial heat transfer capacity and has demonstrated heat transfer coefficients for ammonia in excess of any literature values available for nonboiling heat transfer. This has been done with a relatively coarse circumferential groove

TABLE 4.1 SUMMARY OF HEAT TRANSFER RESULTS

| Parameter | Ammonia | R-11 |
|---|---|---|
| Temperature | 30 ± 10°C | 25 ± 5°C |
| Groove density | 25/cm | 25/cm |
| Open groove heat transfer coefficient | 0.44-0.79 $W/cm^2°K$ (775 to 1390 $Btu/hr-ft^2°F$) | 0.23 $W/cm^2°K$ (405 $Btu/hr-ft^2°F$) |
| Inverted meniscus heat transfer coefficient | 2.67 (4700) | 1.0 (1760) |
| Open groove radial heat flux density | 4 $W/cm^2$ | 1.5 $W/cm^2$ |
| Inverted meniscus heat flux density | 20 $W/cm^2$ | 5 $W/cm^2$ |
| Maximum prime height for open grooves | 6.8 cm | -- |
| Maximum prime height for covered grooves | >15 cm | -- |

of 25/cm. Table 4.2 presents data on grooved evaporator heat transfer coefficients for ammonia and other fluids. This data has been plotted for added clarity as Figure 4.1. In Figure 4.1, the ratio of the overall evaporative heat-transfer coefficient divided by fluid conductivity ($\bar{H}/K_f$) is plotted versus the number of grooves. The factor $\bar{H}/K_f$ is the reciprocal of the effective film thickness. For a given fluid category (ammonia versus halocarbon refrigerants), the effective film thickness for open grooves is approximately inversely proportional to groove density. The inverted meniscus measurements, however, indicate a factor of 4 enhancement in heat transfer over open grooves for the same groove density.

Very significant improvements in evaporative heat transfer surfaces could result from a thorough investigation and understanding of inverted meniscus evaporation. The high heat transfer coefficients measured may be related to vapor-flow-induced film turbulence. Vapor-liquid shear may become a significant factor. However, the fillets are quite small at high watt densities and it is difficult to visualize an effective vapor-liquid interaction which would not be damped out by viscous and surface tension retarding forces.

A second alternative explanation is that fillet inversion creates a fluid film that is thinner overall because of the cup-shaped grooves (see Figure 3.2). In addition, the thinnest portion of the fillet now exists at the base of the groove, rather than at the peaks. The conductive drop in the wall is reduced because heat conduction up the "fin" defined by adjacent grooves is no longer necessary.

Heat fluxes at the fillet interface are high and temperature gradients very large. Although it is easy to show that density-driven convection cells are improbable, there is the possibility that surface tension-driven convection plays a role in heat transfer. The importance of surface tension-driven

TABLE 4.2. TABULATION OF GROOVED SURFACE HEAT TRANSFER DATA

| Grooves/ cm | Fluid | Tempera- ture | $\bar{H}$ | Axial (A) or Circumfer- ential (C)[3] | Wall | Refer- ence | $K_f$ | $\bar{H}/K_f$ |
|---|---|---|---|---|---|---|---|---|
| 8.32 | R-21 | 20°C | 0.114 W/cm$^2$°K | A | Al | 3 | 1.10 mW/cm°K | 104.0 |
| 8.32 | $NH_3$ | 20 | 0.227 | A | Al | 3 | 4.94 | 46.0 |
| 8.32 | R-113 | 20 | 0.0653 | A | Al | 3 | 0.55 | 119.0 |
| 30.3 | $NH_3$ | -23 | 0.7 | A | Al | 2 | 5.90 | 119.0 |
| 30.3 | $C_2H_6$ | -86 | 0.137 | A | Al | 2 | 1.48 | 92.6 |
| 30.3 | $CH_4$ | -153 | 0.173 | A | Al | 2 | 1.77 | 97.7 |
| 30.3 | $O_2$ | -273 | 0.29 | A | Al | 2 | - | - |
| 31.5 | $NH_3$ | 27 | 0.57 | CU | Al | 1 | 4.78 | 119.0 |
| 63.0 | $NH_3$ | 27 | 1.99 | CU | Al | 1 | 4.78 | 416.0 |
| 63.0 | $NH_3$ | 27 | 1.14 | CU | Al | 1 | 4.78 | 238.0 |
| 31.5 | $NH_3$ | 20 | 0.88 | CU | Al | 4 | 4.94 | 178.0 |
| 59.1 | $NH_3$ | 20 | 1.12 | CU | - | 5 | 5.20 | 215.0 |
| 18.9 | $NH_3$ | 20 | 0.91 | V | - | 5 | 5.20 | 175.0 |
| 18.9 | $CH_3OH$ | 20 | 0.43 | V | - | 5 | 2.0 | 86.0 |
| 31.5 | $NH_3$ | 20 | 0.81 | CV | Al | 6 | 4.94 | 164.0 |
| 31.5 | R-21 | 20 | 0.39 | CV | Al | 6 | 1.10 | 354.0 |
| 25.0 | $NH_3$ | 30 | 0.44-0.79 | CU | Al | P[1] | 4.71 | 93-168 |
| 25.0 | $NH_3$ | 30 | 2.67 max | CU | Al | PI[2] | 4.71 | 567.0 |
| 25.0 | R-11 | 30 | 1.0 max | CU | Al | PI[2] | 0.86 | 1160.0 |
| 25.0 | R-11 | 25 | 0.227 | CU | Al | P[1] | 0.87 | 261.0 |

(1) P = Present analysis, open grooves
(2) PI = Present analysis, inverted meniscus
(3) U = Rectangular open cross section
(4) V = V-shape open cross section

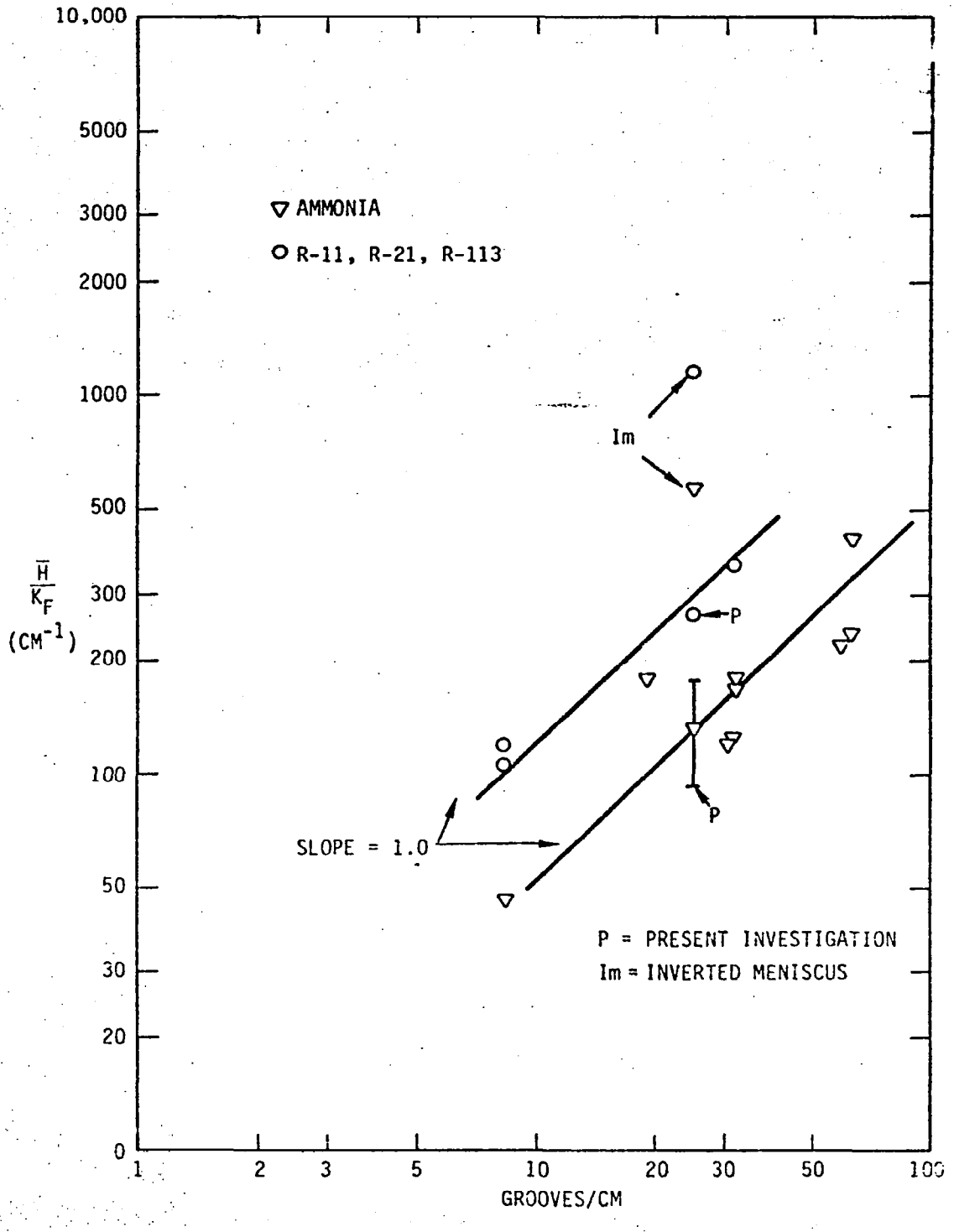


FIGURE 4.1. THE EFFECT OF GROOVE DENSITY ON HEAT TRANSFER COEFFICIENT FOR AMMONIA AND FREONS. HEAT TRANSFER COEFFICIENT IS DIVIDED BY FLUID THERMAL CONDUCTIVITY TO COMPENSATE FOR DATA AT VARIOUS TEMPERATURES. UNUSUALLY HIGH VALUES OF $\bar{H}/K_F$ FOR INVERTED MENISCUS (Im) ARE APPARENT.

convection is correlated by the Marangoni number for thin films of thickness $\delta$

$$N_m = \frac{-\gamma' \delta \rho_f C_p \Delta T_{ev}}{\mu_f K_f} = \frac{-\gamma' \rho_f C_p \Delta T_{ev}^2}{\mu_f Q_a} \qquad (4.1)$$

where $\gamma'$ is the derivative of surface tension with respect to temperature and the heat transfer coefficient is assumed equal to $K_f/\delta$. In a grooved heat pipe the film thickness $\delta$ is quite variable, but if the film is considered to have a uniform thickness over the groove internal wetted perimeter, then a rough estimate of $N_m$ can be made using the equation in $\Delta T_{ev}$ and $Q_a$. On this basis, $N_m$ is in the range 700 to 1400 for ammonia and about 50 to 700 for R-11. Palmer and Berg[8] state the critical Marangoni number is $N_m = 80$ for a film with hydrodynamically free upper boundary and an isothermal lower boundary and constant flux upper boundary. This describes thin-film evaporation very well.

Therefore, since the Marangoni number is as much as 10 times the critical value for convection initiation, this effect cannot be excluded. The experimental data of Palmer and Berg shows an abrupt increase in heat transfer coefficient when convection is driven by differential surface tension. Liquid-film turbulence created by vapor-liquid shear can cause the cells to form by creating an initial disturbance, although differential surface tension is the actual mechanism that maintains the convective cell motion.[8]

To summarize, there are several fundamental explanations for the heat transfer enhancement observed with the inverted meniscus, and each needs to be critically evaluated and related to the experimental data. It is intriguing to speculate on the effect of increasing groove density with the inverted meniscus. If the heat transfer coefficient remains directly proportional to groove density for the inverted meniscus, then attractive gains are possible.

At a groove density of 60/cm, a heat transfer coefficient of 5.34 (9400 Btu/hr-ft$^2$°F) is indicated for ammonia. The maximum flux density would be significantly reduced (see Section 2), but there may remain many useful applications such as in electronic component cooling. Figure 4.2 shows one conceptual idea for cooling an opto-electronic device such as a solid-state laser diode.

In addition to analytical studies of groove operation, it is suggested that empirical tests be implemented to observe changes in heat transfer coefficients and watt density limits as a function of groove density and surface construction.

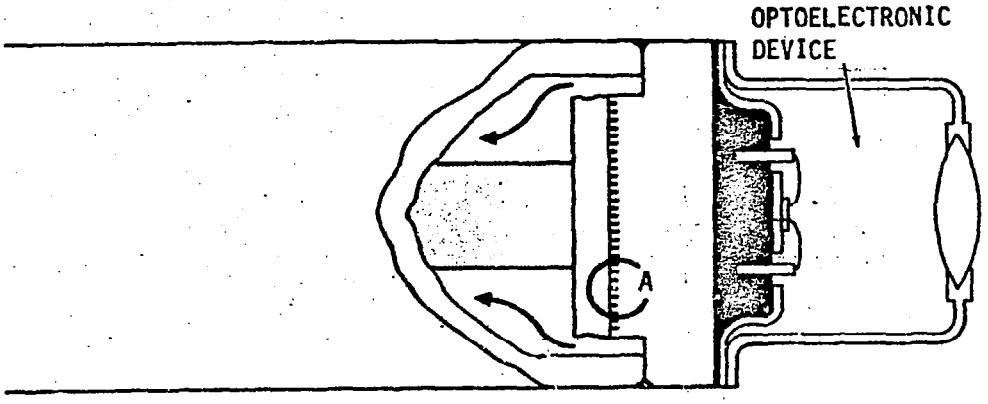


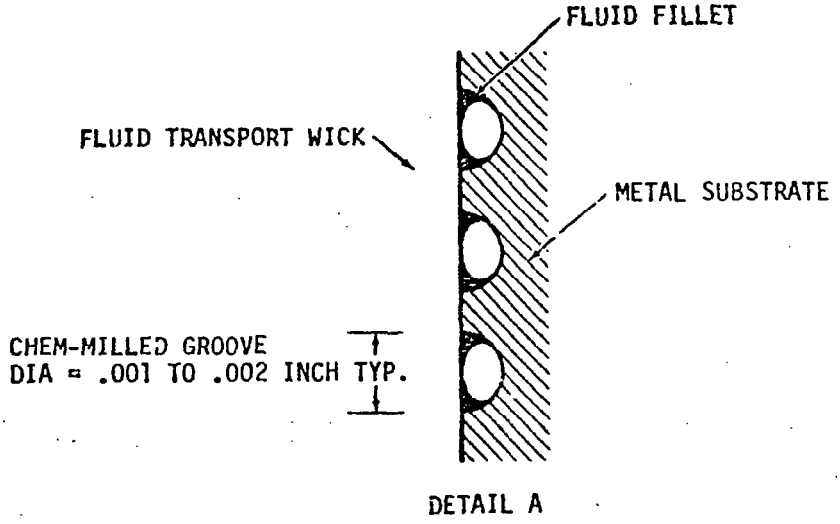


FIGURE 4.2. INVERTED MENISCUS CONCEPT FOR CONCENTRATED HEAT SOURCE, USING HEAT INSERTION THROUGH A MODIFIED END CAP

## 5. REFERENCES


1. B. Kosson et al, "A Tunnel Wick 100,000 Watt-Inch Heat Pipe," 1972 AIAA Thermophysics Conference, San Antonio, Texas. AIAA Paper 72-273.

2. K. Schlitt, J. Kirkpatrick and P. Brennan, "Parametric Performance of Extruded Axial Grooved Heat Pipes from 100° to 300°K," AIAA/ASME 1974 Thermophysics and Heat Transfer Conference, Boston, Mass., 1974. Paper 74-724.

3. N. Kosowski and R. Kosson, "Experimental Performance of Grooved Heat Pipes at Moderate Temperatures," AIAA 6th Thermophysics Conference, Tullahoma, Tenn., 1971. AIAA Paper 71-409.

4. F. Edelstein et al, "Development of a Self-Priming High Capacity Heat Pipe for Flight on OAO-C," 1971 AIAA 6th Thermophysics Conference, Tullahoma, Tenn., 1971.

5. M. Berger and K. Feldman, Jr., "Analysis of Circumferentially Grooved Heat Pipe Evaporators," 1973 ASME Winter Annual Meeting, Detroit, Mich. Paper 73-WA/HT-13.

6. Personal communication, McDonnell Douglas Corp., Reference Memorandum A55-833-B4BA-GDJ-73-29.

7. G. Johnson and E. W. Saaski, "Arterial Wick Heat Pipes," 1972 ASME Winter Annual Meeting, ASME Paper 72-WA/HT-36.

8. H. J. Palmer and J. C. Berg, "Convective Instability in Liquid Pools Heated from Below," J. Fluid Mech., Vol. 47, 1971, p 4, p 779.

# APPENDIX

## Pressure Relations for Evaporator Axial Liquid Flow

The axial transport wick and circumferential wick are assumed to be of constant permeability and it is also assumed that within the evaporator, evaporation is uniform; i.e., the liquid removal rate from the axial transport wick is independent of evaporator position.

If the axial evaporator wick is an artery and arterial flow is laminar, then at any axial evaporator position Z, the volumetric flow rate of fluid $\dot{V}$ is given as

$$\dot{V}(Z) = \frac{\pi R_a^4}{8\mu_f}\left(\frac{dP}{dZ}\right) = \dot{V}_o\left(1 - \frac{Z}{L}\right) \qquad \text{(A-1)}$$

where Z is measured from the condenser end of the evaporator, and where $V_o$ is the volumetric flow rate at Z = 0. If this relationship is integrated from Z = 0 to an arbitrary position Z < L, then

$$\Delta P = \frac{8\mu_f \dot{V}_o}{\pi R_a^4}\left(Z - \frac{Z^2}{2L}\right) = \Delta P_T\left(\frac{2Z}{L} - \left(\frac{Z}{L}\right)^2\right) \qquad \text{(A-2)}$$

where $\Delta P_T$ corresponds to the total evaporator pressure drop. The maximum total liquid pressure drop in the heat pipe is given by $2\gamma/r_c$, and the corresponding maximum heat flux and evaporator pressure drop are termed $Q_m$ and $\Delta P_{em}$, respectively. Then for any fractional power level $Q/Q_m$, the total liquid pressure drop with respect to a constant-pressure vapor phase is

$$\Delta P_{\ell} = \frac{2\gamma}{r_c} \frac{Q}{Q_m} \left\{1 - \pi_e \left[1 - \frac{2Z}{L} + \left(\frac{Z}{L}\right)^2\right]\right\} \quad \text{(A-3)}$$

where $\pi_e$ equals $\Delta P_{em}/(2\gamma/r_c)$.

This is given as equation (5) in Section 2.4.2. At evaporator position Z = o, the liquid pressure drop is

$$\Delta P_{\ell o} = \frac{2\gamma}{r_c} \frac{Q}{Q_m} \left(1 - \pi_e\right) = \frac{Q}{Q_m} \left(\frac{2\gamma}{r_c} - \Delta P_{em}\right) \quad \text{(A-4)}$$

In addition, the liquid pressure drop at the extreme evaporator end is

$$\Delta P_{\ell L} = \frac{2\gamma}{r_c} \left(\frac{Q}{Q_m}\right) \quad \text{(A-5)}$$

as would be expected.

In handling the vapor pressure drop in a groove, the same analytical approach is used, with a uniform vapor injection rate as a function of axial position assumed. For a constant vapor channel cross section and laminar vapor flow, the vapor pressure rise in a single groove, relative to the heat pipe vapor core, is

$$\Delta P_v = \frac{8\gamma}{r_c} \frac{Q}{Q_m} \left[\frac{Z}{L} - \left(\frac{Z}{L}\right)^2\right] \pi_v \quad \text{(A-6)}$$

or

$$\Delta P_v = \frac{2\gamma}{r_c} \frac{Q}{Q_m} \left[1 - \left(\frac{Z}{L}\right)^2\right] \pi_v \quad \text{(A-7)}$$

depending on whether the groove is open or closed at the condenser end, respectively. These are given as equations (6) and (7) of Section 2.4.2.